THE UNIVERSITY OF QUEENSLAND

Development of Novel Perovskite Materials for Oxygen Evolution Reaction

Student Name: Tianyu, LI

Course Code: ENGG 7282

Supervisor: Professor John ZHU & Doctor Xiaoyong XU

Submission date: 30 May 2019

Faculty of Engineering, Architecture and Information Technology

Table of Contents

List of Figures

List of Tables

Abstract

Climate change, especially global warming, which caused by increased concentrations of greenhouse gases in the atmosphere, has become more severe nowadays. When we burn fossil fuels, like coal, oil and natural gas, to create power, we release carbon dioxide pollution into the atmosphere. Worse still, according to the International Energy Outlook report in 2018, the consumption of fossil fuels is expected to keep growing in the following decades with the increasing of the world population. To solve this problem, reducing the amount of electricity generated from fossil fuels and increasing the amount of power from renewable energy sources like wind and solar energy are becoming the trend. These renewables are intermittent and difficult to store in a large scale. Thus, techniques which can store renewables in a large-scale and produce less environmental pollution are required. Electrochemical water splitting has become one of the most promising technologies in recent years because it can produce hydrogen gas as pollution-free fuel from solar energy and other renewables. However, there is a hindrance for electrochemical water splitting system which is the sluggish oxygen evolution reaction. Researches have been carried out to synthesize catalysts for accelerating the reaction. In this project, lanthanum, strontium, cobalt and cerium based perovskite electrocatalysts were synthesized based on the previous study. To investigate and compare their catalytic performance, characterization tests and electrochemical tests were performed. In the end, we found that $La_{0.5}Sr_{0.5}CoO_3$ has the best catalytic performance among six samples and further study is well worth doing to increase the ratio of cerium.

1. Introduction

1.1 World energy status

The usage of fossil fuels has caused significant harm to the environment in the form of greenhouse gas emission and pollution recently. Thus, the using of renewable energy which causes less pollution becomes the trend. According to the International Energy Outlook report in 2018, renewables are expected to be the fast-growing energy source. The energy sources consumption graph is shown in the follows.

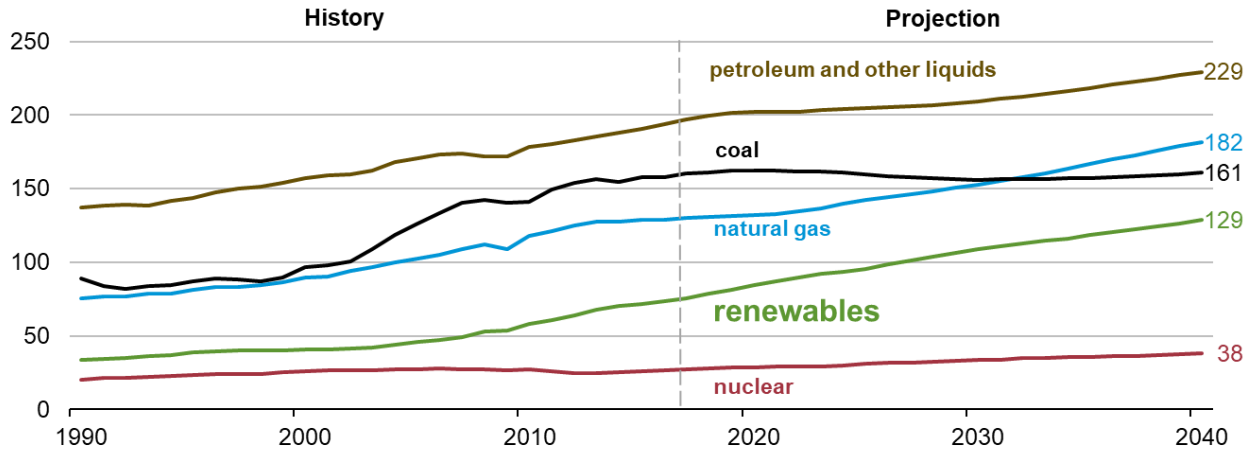

Figure 1. World energy consumption by energy sources (1990-2040)("International Energy Outlook 2018," 2019).

In addition, the demand for energy all over the world will continually grow as the population grows. In this case, technologies to converse and store these intermittent energy sources are important. This specific technology requires a large-scale store of renewables and producing less environmental pollution.

1.2 Water splitting system

Electrochemical water splitting system has become one of the most promising technologies for the past few years because it can produce hydrogen gas as pollution-free fuel from solar energy and other renewables. This conversion progress can be achieved both directly and indirectly

(Man et al., 2011). The direct way is to excite electrons in a semiconductor by photos when the valence band has the low energy level, and the indirect way is to electrolyte water by potential difference from a wind turbine or photovoltaic cell (Man et al., 2011).

The diagram of typical water splitting system shows in the following picture. The system has three general components, which are anode, cathode and electrolyte. Water molecules are split and oxygen and hydrogen are released when the external voltage applied to the system.

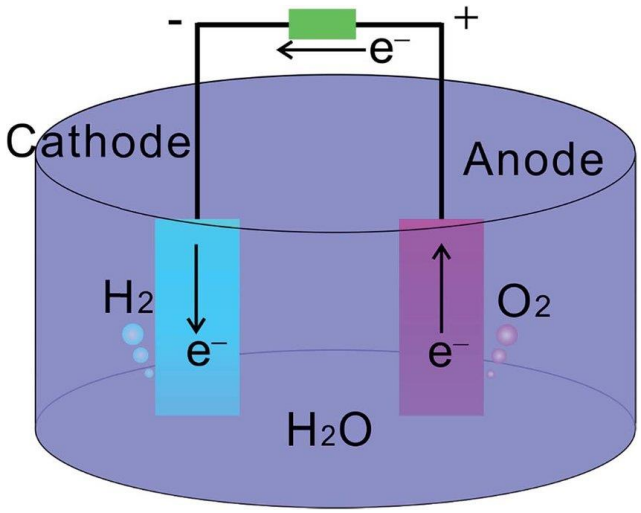

Figure 2. Typical electrochemical water splitting system schematic(Peng et al., 2019).

Lee et al. introduced a new concept about water splitting system which is the solar water splitting combined with reverse electrodialysis (RED). Since the photoelectrochemical (PEC) water splitting has the issues about its stability and efficiency, they produced the RED to provide a flexible selection for photoelectrode material, like the inexpensive materials with a narrow band gap, which makes more cost-effective practical use for water splitting possible. As shown in Figure 3, a PEC-RED system was integrated using single-junction Si photoelectrode and RED stack instead of traditional proton selective membrane to split water via solar energy without any external bias (J. Lee et al., 2017).

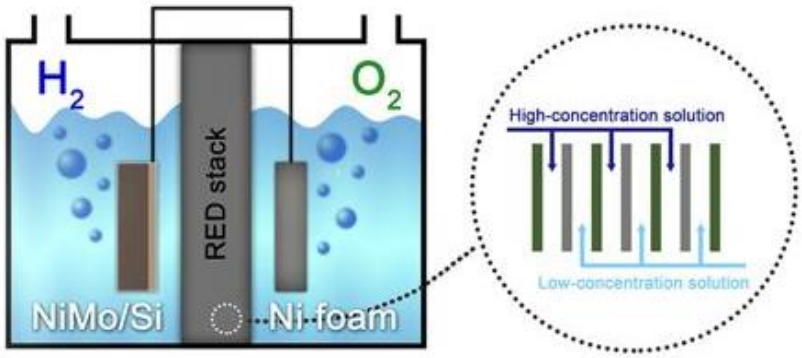

Figure 3. Integrated PEC-RED system (J. Lee et al., 2017).

As mentioned above, there are direct and indirect methods to achieve water splitting and both of them have two half-reactions, including anodic oxygen evolution reaction (OER) and cathodic hydrogen evolution reaction (HER). The overall reaction and half reactions can be represented as follows:

Overall: $2H_2O \rightarrow 2H_2 + O_2$ (1)

Anode: (2)

$$4OH^- \rightarrow 2H_2O + O_2 + 4e^- \ (alkaline\ or\ neutral\ solution)$$

$$2H_2O \rightarrow 4H^+ + O_2 + 4e^- \ (acid\ solution)$$

Cathode: (3)

$$4H_2O + 4e^- \rightarrow 2H_2 + 4OH^- (alkaline\ or\ neutral\ solution)$$

$$4H^+ + 4e^- \rightarrow 2H_2 \ (acid\ solution)$$

Four electrons are required to produce an oxygen molecule in the anodic OER. However, there is a problem for OER. The process of OER could be divided into several steps and each step transfers only one electron (J. Lee et al., 2017). Thus, anodic OER is extremely sluggish that results in a low efficiency for the whole system. To solve this problem, OER catalysts are used.

1.3 Parameters in water splitting system

1.3.1 Electrode

Electrode plays an important part in OER performance testing. A different structure, material and access of catalyst to the electrolyte of the electrode can affect the reaction rate (Tahir et al., 2017). There are two types of electrode divided by support including a flat surface electrode and 3D electrode. Glassy carbon and gold electrode are flat surface electrodes, and carbon cloth/paper belongs to 3D electrodes (Tahir et al., 2017). The pictures of them are shown in Figure 4 and Figure 5, resepectively.

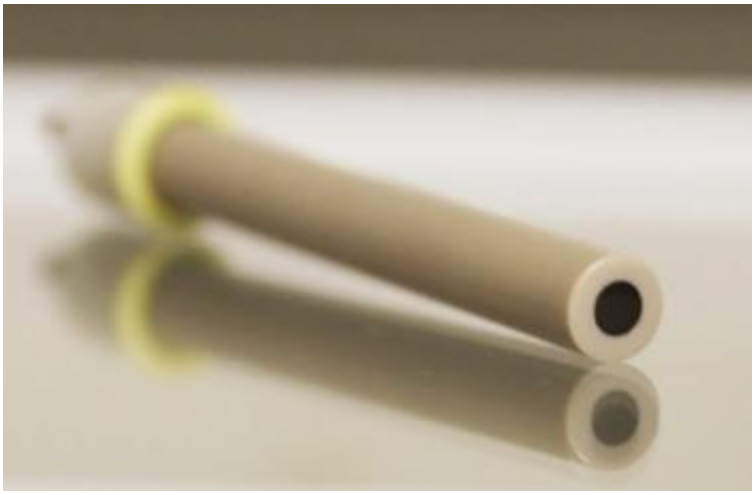

Figure 4. Glassy carbon disk electrode("Working Electrode - GC Glassy Carbon Disk Electrode ", 2019).

Figure 5. Carbon cloth electrode (Arungovind, Purushotham, Arunkumar, & Sendilvelan, 2017).

One more thing needs to notice about the choice of the electrode is that some electrode may alter the OER performance of powder catalysts (Browne & Mills, 2018). Some studies have proved that the bad OER performance for some catalysts due to the underlying support (Oh et al., 2016).

1.3.2 Electrolyte

The other fact can get from the reaction formula of water splitting that acid and alkaline solution can inflation the performance of electrode materials, which is also to say that different electrolytes make OER performance different. OER electrocatalysis performance better in the alkaline environment than acid and neutral solution. Most OER electrocatalysts are unstable in acid solution because of the high oxidation potential. Thus catalysts that can work in a large range of pH value are desirable (Tahir et al., 2017).

1.3.3 Overpotential (η)

There is a vital parameter to evaluate OER performance of catalysts, which is overpotential. Under ideal condition, the reaction needs applying a potential equal to the potential at its equilibrium state to drive it. However, the applied potential should be higher to overcome other kinetic barrier in the real world (Suen et al., 2017). The overpotential is the potential difference between ideal potential and potential observed in the experimental condition. Overpotential can reflect the cell voltage efficiency directly. The applied potential can be calculated using the Nernst Equation and has the formulation:

$$E = E^{0'} + \frac{RT}{nF} ln \frac{C_o}{C_R} \quad (4)$$

Where E is the applied potential, $E^{0'}$ is the potential of the whole reaction, R and F are constants, T is absolute temperature, n is the number of transferred electrons, and C_o and C_R are the

concentration of oxidations and reductions respectively (Suen et al., 2017). Thus, the overpotential can get as:

$$\eta = E - E_{eq} \tag{5}$$

In which E_{eq} is the potential at equilibrium state. For the OER overpotential calculation, E_{eq} is regarded as 1.23 V. In this case, the ideal OER electrocatalysts require a low overpotential.

1.3.4 Exchange current density (i_o)

Another important indicator in the OER is the exchange current density, which is a parameter used in the Tafel equation. Exchange current is the rate of reaction at the equilibrium electrode and the density of exchange current can be defined as the current density flows in both directions ("Exchange Current Density," 2019). Thus, the larger exchange the exchange current, the faster the reaction. In this case, the ideal OER electrocatalysts require a high exchange current density. The calculation formulas of i_0 are (Suen et al., 2017):

$$i_0 = {}^{j_0}/_{A} \tag{6}$$

$$j = j_a + j_c \tag{7}$$

$$j_a = nFk_a[C_R]\exp(\frac{\alpha_a nFE}{RT}) \tag{8}$$

$$j_c = nFk_c[C_O]\exp(-\frac{\alpha_c nFE}{RT}) \tag{9}$$

Where j_a and j_c are the anodic and cathodic currents and j_0 is the exchange current. At equilibrium state, j_a equals to j_c and E equals to E_{eq}. A is the area of the electrode.

1.3.5 Tafel equation and slope (b)

Tafel equation is an equation that reveals the relationship between the rate of reaction and its overpotential which is named after Julius Tafel ("Tafel equation," 2019). The Tafel equation for a single electrode can be presented as:

$$\eta = A \times log(\frac{i}{i_0}) \tag{10}$$

Where η is the overpotential, i is the current density (A/m^2) and i_0 is the exchange current density, as mentioned above. In this equation, A is the Tafel slope which means "how fast the current increases against overpotential" (Suen et al., 2017).

In the Tafel slop, the overpotential is on the y-axis and current density is on the x-axis. Thus, for the OER catalysts with good performance, they should have a large current density and a low Tafel slope.

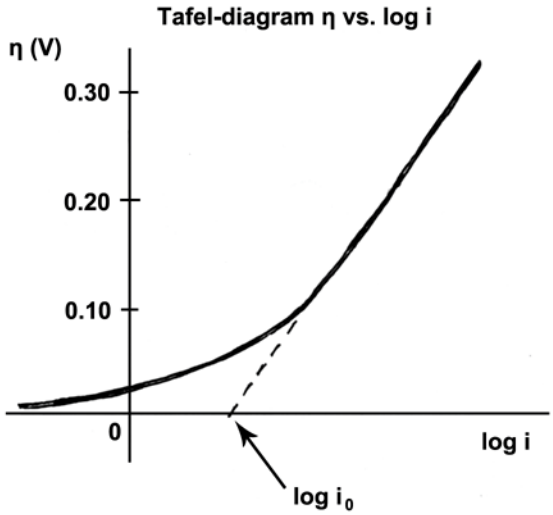

Figure 6. Tafel plot example("Tafel equation," 2019).

1.3.6 Stability

Stability is an important criterion for OER electrocatalysts to compare their performance. The stability of catalysts affects various factors, for example, the pH value of electrolyte. Some

catalysts are not stable in acid solution but have a good performance in basic solution. Moreover, the nature of the electrode is also an important factor for stability. Normally, the electrode which is pasted on active materials presents worse stability than the one which is fabricated on the active materials directly (Tahir et al., 2017). Most researches use the chronopotentiometry test in an electrochemical experiment to test the stability of materials.

1.3.7 Activity

In addition, mass activity is also an important parameter to evaluate the quality of electrocatalysts (Tahir et al., 2017). The mass activity can be calculated as the current density at a given potential divided by the mass loading on the working electrode.

1.4 Hydrogen evolution reaction (HER) in Water splitting system

HER is a process to produce hydrogen. There are two general ways nowadays to achieve this. One is the industrial way to produce hydrogen by reforming natural gas, which is the main way to obtain hydrogen and has the following reaction(Wang, 2012):

$$CH_4 + H_2O \rightarrow CO + 3H_2 \quad (11)$$

However, the most familiar way for most people is the water splitting. Even though the lowest voltage for splitting water to hydrogen and oxygen is 1.23 V according to the kinetic calculation, higher voltage is needed depending on different electrode used(Wang, 2012). For the catalysts of HER, platinum is the best one with a large current and a small Tafel slop as we know so far(Conway & Tilak, 2002).

In general, HER process has main steps as follows (Yan, Xia, Zhao, & Wang, 2016):

Firstly, electrochemical hydrogen adsorption step has the following equations,

$$H_2O + e^- + M \rightarrow MH_{ads} + 4OH^- \ (alkaline\ or\ neutral\ solution) \quad (12)$$

$$H^+ + e^- + M \rightarrow MH_{ads} \ (acid\ solution) \quad (13)$$

In the first step, protons form solutions are attached on the surface of the catalysts. Then the electrons from electrode combine with protons to form MH_{ads}.

Next step is electrochemical desorption,

$$MH_{ads} + H_2O + e^- \rightarrow M + OH^- + H_2(alkaline\ or\ neutral\ solution) \quad (14)$$

$$MH_{ads} + H^+ + e^- \rightarrow M + H_2(acid\ solution) \quad (15)$$

Or the chemical desorption,

$$2MH_{ads} \rightarrow 2M + H_2 \quad (16)$$

In this step, desorption happens on the electrode and hydrogen leave the site of the electrode.

One of the two steps can determine the total rate of HER depending on different HER catalysts. For platinum, the rate determined step is the electrochemical desorption because the Gibbs free energy of it is raised (Wang, 2012). While for another catalyst named MoS_2, the rate determined step is the electrochemical hydrogen adsorption step(Wang, 2012). The MoS_2 which has a hexagonal structure is also an attractive catalyst for HER.

1.5 Oxygen evolution reaction (OER) in Water splitting system

As mentioned above, the process of HER has just two electron transference, while OER is a reaction with four electron-proton coupled (Lyu, Wang, Choi, & Yin, 2019). Hence it is speculated that OER needs higher overpotential to occur. Like MH forms in HER, there is MO formed in OER. Two main approaches can achieve this, which are the direct route and indirect route shown in the figure below (Lyu et al., 2019).

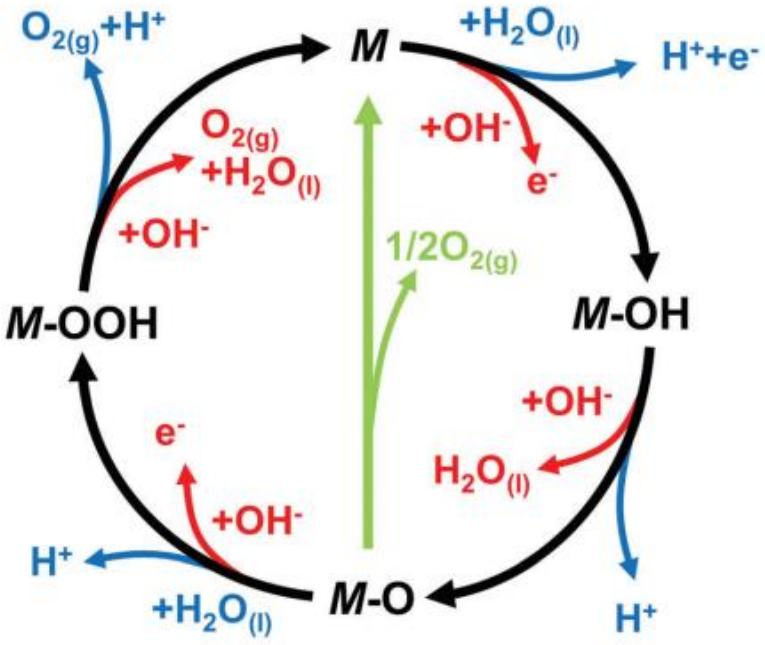

Figure 7. The mechanism for OER (Lyu et al., 2019).

The green route is the direct way, and the black route is the indirect way with a blue line in acid and red line in alkaline solution. According to the study of Suen et al., the proposed reactions in acid solutions are:

$$M + H_2O \rightarrow MOH + H^+ + e^- \quad (17)$$

$$MOH + OH^- \rightarrow MO + H_2O + e^- \quad (18)$$

$$MO \rightarrow O_2 + M \quad (19)$$

$$MO + H_2O \rightarrow MOOH + H^+ + e^- \quad (20)$$

$$MOOH + H_2O \rightarrow M + O_2 + H^+ + e^- \quad (21)$$

And the reactions in alkaline are:

$$M + OH^- \rightarrow MOH \quad (22)$$

$$MOH + OH^- \rightarrow MO + H_2O + e^- \quad (23)$$

$$MO \rightarrow O_2 + M \quad (24)$$

$$MO + OH^- \rightarrow MOOH + e^- \quad (25)$$

$$MOOH + OH^- \rightarrow M + O_2 + H_2O + e^- \quad (26)$$

1.6 Noble metal-based OER catalysts

Researched have done about the discovery of OER catalysts for many years. In the previous, noble metal-based oxides such as RuO_2 and IrO_2 mixed with TaO_2 were used as the best OER catalysts in terms of their activity and stability under a wide range of pH value.

Among these noble metal-based oxides, RuO_2 is considered as the most active catalysts for the OER performance in an acid environment and IrO_2 is the second one which is used in the proton exchange membrane water electrolysers because of its excellent durability (Z. Ma et al., 2018).

OER kinetic of the noble metal-based oxides can be described by the reaction energies. Take the study of Ma et al. as an example. They used *OH*H phased as the energy reference because of its lowest energy state to compare. The results show in the follows. The *O is the most

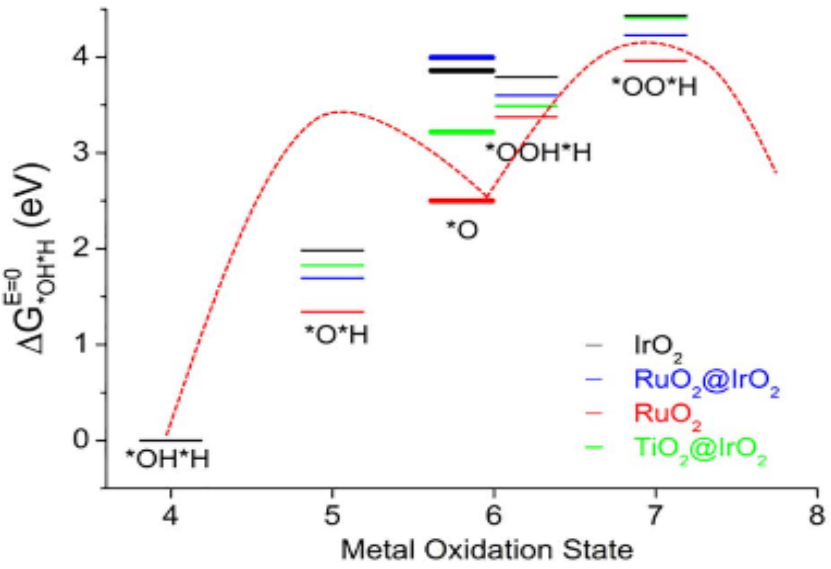

Figure 8. OER kinetic compare (Z. Ma et al., 2018).

significant element because it is the precursor of the O-O band. From the results, we can get

that the o adsorption for IrO2 monolayer is weakened by RuO2 substrate while strengthened by TiO2.

Forgie has reported that bimetallic Ru with other metals shows an improved OER performance (Forgie, Bugosh, Neyerlin, Liu, & Strasser, 2010). They synthesized binary Ru-M alloy catalysts using combinatorial synthesis and proved that cubic Ru-Co electrocatalysts with reduced content of Ru have a higher OER performance for the electrolytic water splitting compared with benchmark Ru.

Lee et al. synthesized r-IrO_2 and r-RuO_2 nanoparticles and tested their OER performance in both alkaline and acid solutions. The results show that r-RuO_2 nanoparticles have a better performance and these nanoparticles perform higher stability than commercial ruthenium and iridium combined with carbon catalysts (Y. Lee, Suntivich, May, Perry, & Shao-Horn, 2012).

Furthermore, to enhance improve the stability and activity of the noble metal-based catalysts, Li et al. combined the excellent stability of IrO_2 and the outstanding activity of RuO_2 to synthesize ruthenium-iridium bimetallic oxides as the OER catalyst named IrO_2-RuO_2@Ru (3:1) (Li, Li, Ge, Liu, & Xing, 2017). This catalyst shows an advantage that can reduce the use amount of noble metals and have a good OER performance.

There is another study about the noble mental catalysts from the study of Ma Et al. Ma used carbon-supported ruthenium as template coated with iridium to synthesize RuO_2@IrO_2-core-shell nanocatalysts to improve the OER performance of IrO_2-based catalysts. Even though the sample is not ideal as it reduces *O adsorption strength slightly, this study improved that the synthesis method is flexible for the water-splitting catalysts and can be used by changing metal oxides to achieve better OER performance (Z. Ma et al., 2018).

Similar to the last study, Audichon et al. synthesized a core-shell-like IrO_2@RuO_2 through surface modification method in ethanol medium. The schematic diagram shows below.

Compared with pure RuO_2 and pure IrO_2, IrO_2@RuO_2 shows the highest activity as the intimate contact between the two pure oxides boost a synergistic effect. This study also provides a design method for the enhancing of efficiency and stability to the water-splitting catalysts (Audichon et al., 2016).

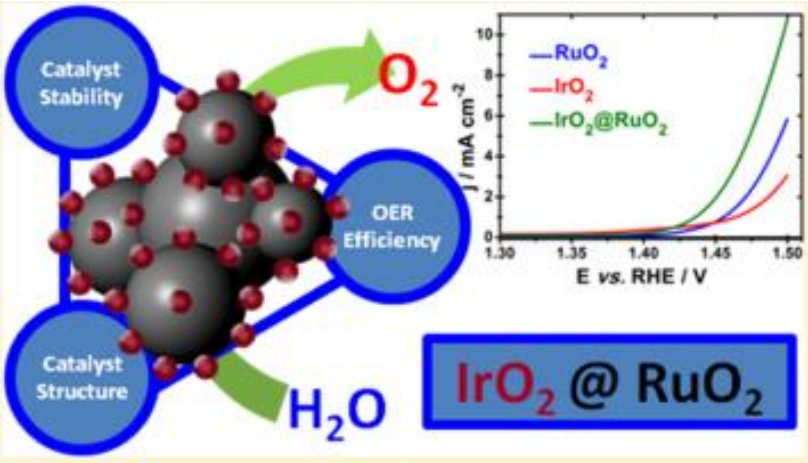

Figure 9. Schematic diagram of IrO2@RuO2 (Audichon et al., 2016).

However, there is an obvious hindrance for the large-scale use of those noble metal-based catalysts which is the high price. In this case, numerous researches have been carried out to synthesize other metal elements oxides to find the catalysts with high efficiency, good stability and low price.

1.6 Earth-abundant metal oxides and perovskite-type catalysts

Because the water-splitting system requires catalysts to accelerate both anodic and cathodic reactions as mentioned above, the non-precious electrocatalysts have activity and effectivity for both of them which are called bifunctional heterogeneous water-splitting electrocatalysts. The examples for catalysts are like transition metal sulphides for HER and transition metal oxides for OER (Yan et al., 2016).

For the ideal design, OER and ORR happen in same pH environment so that they can work together. Moreover, the pH environment is better to be strong acid or alkaline because these

this kind of condition can decrease the overpotentials of the electrocatalysis system (Yan et al., 2016).

Transition metal oxides and perovskites are convinced as the electrocatalysts with best performance to replace the expensive noble metal oxides in some studies (Cheng & Chen, 2012; Choi et al., 2014). Because of their abundance and high OER performance, perovskites have been used in the area of fuel cells and metal-air batteries (Shin, 2016).

It is approved that A-sites influence oxygen adsorption and B-sites influence the activity of adsorbed oxygen (H. M. Zhang, Shimizu, Teraoka, Miura, & Yamazoe, 1989). And Yamada et al. proved that cobalt ions for substituting in B-sites increase the activities because the cobalt ions have a high oxidation state. The activities of cobalt-containing oxides are influenced by the property of additional metal ions without redox activity which is also important for the development of electrocatalysts with high OER performance (Yamada, Yano, Hong, & Fukuzumi, 2012). Strontium and lanthanum ions for substituting in A-sites enhance the catalytic activity, conductivity and oxygen dissociation ability for OER (H. M. Zhang et al., 1989).

In this basis, Shin et al. synthesized lanthanum and cobalt oxides and compared their performance for air electrode in Li-air battery. The results show that LaCoO3 has a high catalytic activity for OER, and they also used strontium to substitute lanthanum in A-sites to improve its electrocatalytic activity for both ORR and OER. They have successfully improved that perovskites are perfect materials for the Li-air battery cathodes.

Moreover, the fist-row transition metals are also received extensive attention (Hunter, Gray, & Muller, 2016). Researches have been performed to investigate the birnessite manganese oxides synthesized with intercalated divalent cations (Wiechen, Zaharieva, Dau, & Kurz, 2012). The results show that calcium ions have better influence than strontium and magnesium ions, and also the activity of manganese oxides are affected by the oxidation methods.

In addition, iron oxides were studied deeply because of its low cost and a large amount (Hunter et al., 2016). For example, α-Fe_2O_3 shows excellent stability but a low conversion efficiency and the amorphous Fe_2O_3 has a better oxidation activity (Awad, Ashour, & Allam, 2014; Smith, Prévot, Fagan, & Zhang, 2013). However, after doping silicon in Fe_2O_3, the perovskite shows a higher conversion efficiency (Cesar, Kay, Gonzalez Martinez, & Gratzel, 2006).

It is difficult to find a general method to synthesize electrochemical catalysts with excellent OER performance. However, the composition and particle size are certainly important. A large number of studies have provided good examples and thoughts for the future direction.

1.7 Mechanism of characterization and electrochemical tests

Characterization tools are significant in material-based research. For now, there are plenty of scientific technologies help us to study the properties of materials. The properties of materials include, but not limited to the structure, morphology, chemical analysis and spectroscopic characterization(Sharma, Verma, Khan, Kumar, & Khan, 2008). Characterization tool can be divided into three general groups which are microscopy, spectroscopy and macroscopic testing("Characterization (materials science)," 2019). Microscopy is the technique group used to investigate the surface and subsurface of the materials which can use photos or electrons to gather the surface data on a range of scale. The techniques group of spectroscopy are used to get the information of chemical compositions, crystal structure and photoelectric properties of the materials. And the last macroscopic testing is used to characterize macroscopic properties. The techniques that have been used in this project are introduced in the follows.

1.7.1 X-ray Powder Diffraction (XRD)

X-ray powder diffraction is one of the spectroscopy methods used to determine the crystal structure of materials. The tested sample should be ground well, homogenized and average bulk (Dutrow & Clark, 2019). The X-ray diffraction is based on the interference of X-rays and

crystalline samples, where X-rays generated by a cathode ray tube can diffract into specific directions to samples. Then the samples will produce constructive interference under the rule of Bragg's Law, which is:

$$n\lambda = 2d\ sin\theta \tag{27}$$

Where n is an integer, λ the wavelength of beam, d is the spacing between diffracting planes, and θ is the incident angle. The schematic diagram is as follows.

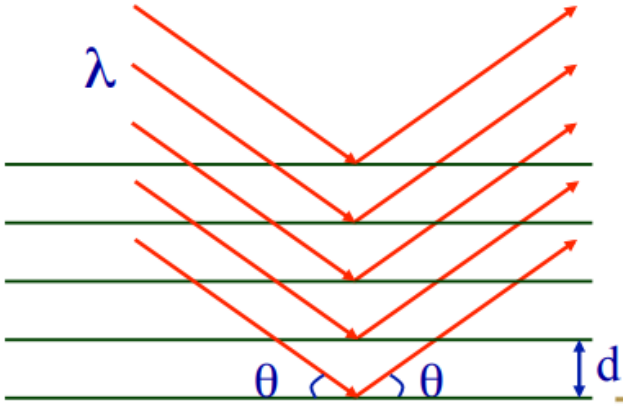

Figure 10. Schematic diagram of Bragg's Law (Zou, 2018)

After generated by the cathode ray tube, X-rays are filtered become monochromatic radiation and collimated to concentrate directing to samples. Thus, in the simplest instance, the XRD experience includes diffracted intensities and angles observed to form an XRD pattern. This pattern can be considered as a chemical identification after comparing the pattern with a database of known patterns("X-ray diffraction," 2019).

The normal uses of XRD are determining unit cell dimensions, measuring sample purity and characterization crystalline materials. With specific technologies applied on XRD, it also can be used to determining crystal structures (Rietveld refinement), determining modal amounts of minerals (quantitative analysis) and so on (Dutrow & Clark, 2019). XRD is a powerful and efficient way to identify an unknown mineral. However, limitations still exist, for example, the

samples must be grounded into powder, and peak may be overlay because of high angle reflections (Dutrow & Clark, 2019).

As for the data analysis, the resulted patterns are generally presented as peak positions 2θ in x-axis and X-ray counts as the y-axis. The intensity is reported as the peak height intensity. Then, d-spacing can be calculated from the appropriate value of λ using Bragg's law equation (27). D-spacing is unique for every mineral, so compare calculated data with the database can identify the unknown sample.

1.7.2 X-ray photoelectron spectroscopy (XPS)

XPS is another one of the spectroscopy methods used to measure the elemental composition. There are numerous surface analysis techniques, such as SAM, SIMS, AFM, XPS, etc. The most popular one is XPS, which is also known as Electron Spectroscopy for Chemical Analysis (ESCA). XPS is a useful technique because it not only can give the information of element composition, but also provide the information of the electronic state of elements. For example, for the perovskite-type catalysts with cobalt, compared with trivalent cobalt, bivalent cobalt contributes to the forming of oxygen vacancies which are helpful to improve the OER performance. So that, XPS can be used to analyse the ration of bivalent with trivalent cobalt to speculate the OER performance. Since XPS is a surface analysis technique, the average depth of analysis for its measurement is about 5 nm.

The basic principle of a XPS is accomplished by exciting the surface of a sample with the Al kα X-rays causing photoelectrons to be emitted from the surface. Then, electron energy analyser measures the energy of these emitted photoelectrons which can provide bonding energy and intensity for determining elements. The schematic diagrams of the emitted photoelectrons show as follows. The emitted photoelectrons have low kinetic energy and thus have a mean free path of only about 3 nm. The calculation of kinetic energy shows in equation 28.

$$KE = h\nu - BE - \phi \quad (28)$$

Where *KE* is kinetic energy, $h\nu$ is X-ray energy, *BE* is binding energy, and ϕ is work function.

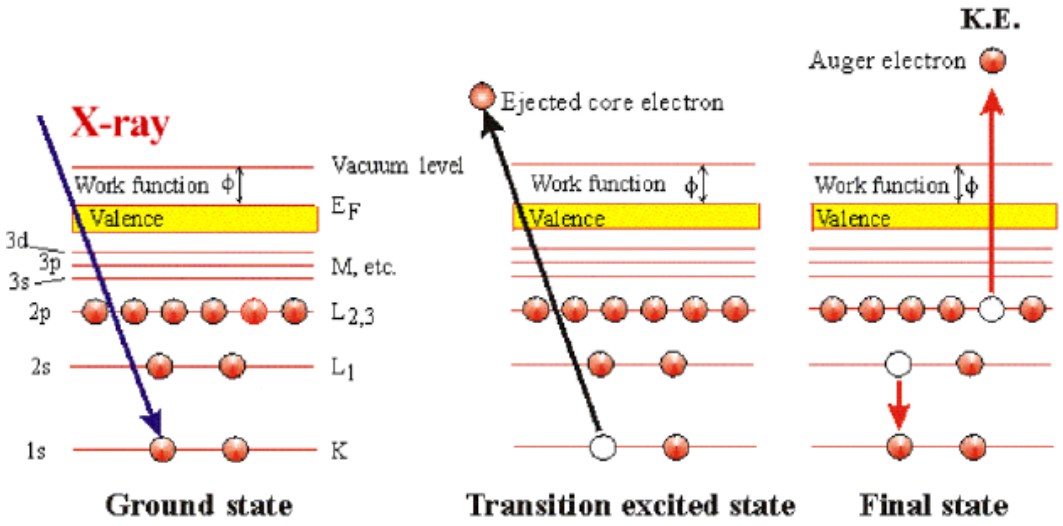

Figure 11. Interaction of X-ray with electrons causing ejection of photo and Auger electrons(Zou, 2018).

Kinetic energy is independent to X-ray energy, however, the Auger peak positions depend on the x-ray source.

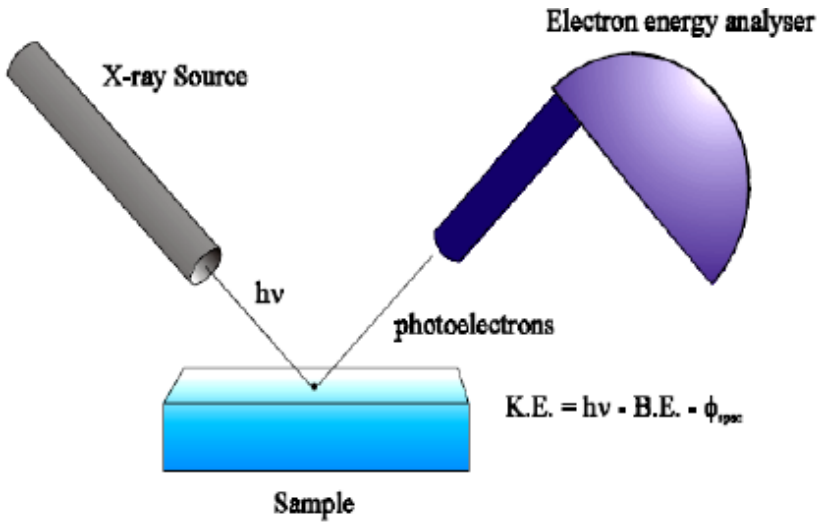

Figure 12. Schematic diagram of XPS(Zou, 2018).

For the analysis of the XPS spectrum, peaks in the spectrum which get from the photoelectrons without energy loss are used to identify the elements. The background is from the photoelectrons with energy loss. Take the peaks of Au, for example. The p, d and f orbits can

be observed in two peaks. They have different area ration. For p orbits, the peaks ration is: $2p_{3/2}: 2p_{1/2} = 2:1$. For d orbits, the peaks ration is: $3d_{5/2}: 3d_{3/2} = 3:2$. For f orbits, the peaks ration is: $4f_{7/2}: 4f_{5/2} = 4:3$. The separation between the two peaks is spin-orbital splitting, and its values of a core level for a specific element are similar. Same to the spin-orbital splitting, the peak area ratios of a specific element are also similar. In this case, the spin-orbital splitting and peak area ration of p, d and f orbits can be used to identify elements(Smart & McIntyre, 2019).

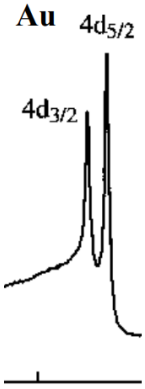

Figure 13. Peaks of Au in the XPS spectrum(Smart & McIntyre, 2019).

However, there is a limitation for XPS, which is the analysis depth. Compared with EDAX which has an analysis depth range with 1000-5000 nm, XPS just has the range of 2-10 nm.

Apart from the functions mentioned above, XPS is a powerful tool for solving many industrial problems, for example, analysing metals corrosion, contamination and discolourations.

1.7.3 Brunauer-Emmett-Teller (BET) surface area

BET theory is used to measure the surface area of materials, including the pore size distribution using physical adsorption of gas molecules on a solid surface. The amount of adsorbed gas is related to the exposed surface of materials and also the temperature, pressure and strength of the interaction between gas and solid(Raja & Barron, 2019). Nitrogen is commonly used in the BET test because of its excellent properties for the test.

The area is calculated by the amount of adsorbed gas corresponding to the monomolecular layer on the surface. The BET theory is based on Langmuir theory, so there are some hypotheses used for the calculation("BET theory," 2019):

- Infinite gas molecules adsorption in layers;
- Langmuir theory works for every layer; and
- Interactions happen only between adjacent layers.

There are five types of adsorption isotherms when it comes to collecting data according to the relationship between the amount of adsorbed gas with pressure and the five types of isotherm plots are shown in the following.

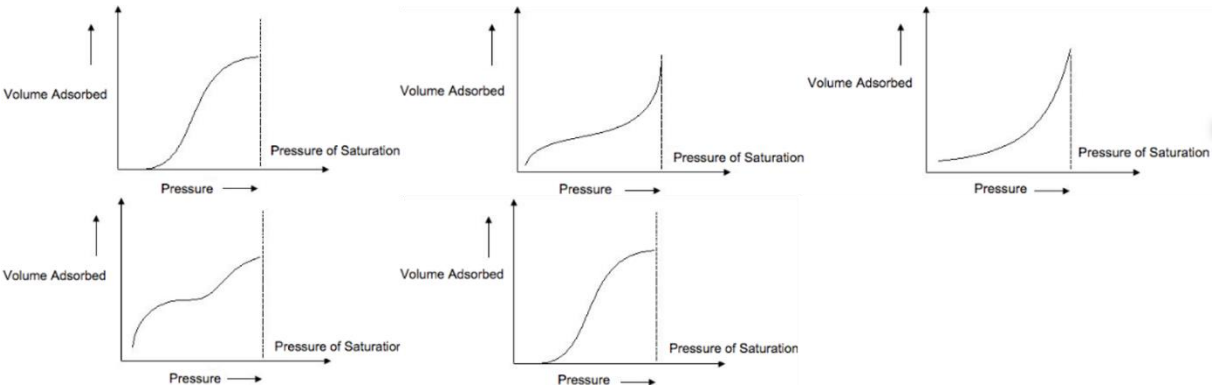

Figure 14. Five types of isotherm plots in BET test(Raja & Barron, 2019).

According to the hypotheses, the calculated equation is as follows("BET theory," 2019):

$$\frac{1}{v(p_0/p-1)} = \frac{c-1}{v_m c}\frac{p}{p_0}\frac{1}{v_m c} \tag{29}$$

Where p_0 is the saturation pressure and p is the equilibrium pressure of adsorbents, v is the volume of adsorbed gas and v_m is the adsorbed gas quantity. As the BET constant, c has a relationship with the heat of adsorption for each layer (E_1 is the heat for the first layer and E_L is the heat for the second and higher layers)("BET theory," 2019).

$$c = \exp\left(\frac{E_1 - E_L}{RT}\right) \tag{30}$$

So the total surface S_{total} and specific surface S_{BET} can be calculated as

$$S_{total} = \frac{v_m N s}{V} \tag{31}$$

$$S_{BET} = \frac{S_{total}}{a} \tag{32}$$

Where *a* is the mass of the sample.

Moreover, before testing BET surface area of samples, samples should be degassed in the glass tubes to minimize the influence of air firstly. After degassing, the samples are removed to analysis place, and liquid nitrogen is used to keep the test in low temperature so that the interaction between gas and solid can be strong enough for the amount of adsorbed gas measurement(Raja & Barron, 2019).

However, compared to NMR, which is also a technique testing surface area, BET test can just be used to calculate the surface area of fry powers and need a long time to adsorb gas molecules (Raja & Barron, 2019).

1.7.4 Rotating ring-disk electrode (RRDE) electrochemical test

RRDE is the technique applying in catalyst evaluation to test OER and ORR performance which has two electrodes. It can be telling from its name that similar to rotating disk electrode (RDE), RRDE has disk electrode in the centre, but has one more ring electrode surrounding the centred disk electrode. The picture of working electrodes of RRDE show in below.

Figure 15. The picture of different catalogues of working electrodes ("Rotating Ring Disk Electrode (RRDE)," 2019)

During the measurement, the samples are loaded on the centred disk electrode, and two electrodes rotate in the same rate.

Because RRDE has one more ring electrode than RDE, and two working electrodes are electrically isolated, RRDE has an advantage in testing multielectron processes (Jia, Yin, & Zhang, 2014). There is a detailed schematic diagram of working electrodes in the follows.

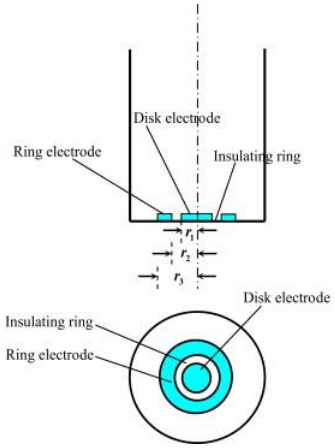

Figure 16. Schematic diagram of two working electrode on RRDE(Jia et al., 2014).

As shown in Figure 16, r_1, r_2 and r_3 are important parameters in the RRDE system. A non-conductive ring separates two electrodes. The ring can be used as a detector to analyse disk reaction products and intermediates. For example, to study the ORR mechanism, the intermediates produced by reaction happened on disk electrode can be thrown to the ring

surface. Then the ring can oxide or reduce the product and generate ring current which can be detected its quantity (Jia et al., 2014).

Similar to RDE, RRDE uses three kinds of materials to its working electrodes which are platinum, gold and glassy carbon because of their high stability. Thus, there are commonly nine combinations of ring-disk electrodes for specific usages (Raja & Barron, 2019). Also, there are different geometric sizes of the electrodes to fit the requirements of studies.

Moreover, the surface of electrodes needs to be kept clean and quite plain for the uniform and controllable hydrodynamic condition. Thus, polishing powders and polishing paper are used for the polishing of the surface of electrodes and polishing needs to be processed with care. Most of the electrodes just need alumina powder to remove the containment and be cleaned by sonicator in ethanol solution.

Figure 17. Picture of RRDE equipment (BioLogic, 2019).

1.8 Summary

Technologies to storage renewable energies on a large scale are imminently needed nowadays. Water splitting system is one of the promising technique. Perovskite-type catalysts which synthesized by earth-abundant metals are ideal for the water-splitting system because of their high performance and low price. To evaluate their performance, XRD can be perfprmed to

determine the crystal structure of materials, XPS can be used to determine the surface elemental compositions, and RRDE is operated to compare their OER and ORR performance.

2. Objectives

According to the literature, perovskite-type electrocatalysts are the development trend. Lanthanum, strontium and cobalt have good performance in the catalysis of oxygen evolution reaction and cerium doping might be a worthwhile approach. Thus, in this project, firstly, we are going to synthesize lanthanum, strontium and cobalt-based perovskite electrocatalysts with different ratio and choose one with the best performance using characterization tests, which are XRD and XPS, and RRDE electrochemical test. Then doping cerium with different ration into the best performance sample and investigate the changes of OER performance. The conclusion will be obtained according to the performance of three cerium doping samples.

3. Experimental

3.1 Synthesis

The synthetic method of six samples was the EDTA-citrate complexing method. The raw chemicals that used in this experiment were all analytical reagent. The chemicals and their labels are listed in the follows.

Table 1 Chemical labels

Chemicals	Formula	MW	Purity	Form	Company
Lanthanum(III) nitrate hexahydrate	$La(NO_3)_3 \cdot 6H_2O$	433.01	99.9%	Crystalline	Alfa Aesar
Lanthanum(III) nitrate hydrate	$La(NO_3)_3 \cdot xH_2O$	324.92	99.9%	Powder and chunks	Aldrich
Strontium	$Sr(NO_3)_2$	211.63	99.0%	Powder	Chem-supply
Cobalt(II) nitrate hexahydrate	$Co(NO_3)_2 \cdot 6H_2O$	291.03	99.5%	Wet crystalline aggregates	Wako Pure
Cerium(III) nitrate hexahydrate	$Ce(NO_3)_3 \cdot 6H_2O$	434.23	99.5%	Crystalline aggregates	Alfa Aesar
EDTA di-SODIUM salt	$C_{10}H_{14}N_2Na_2O_8 \cdot 2H_2O$	372.24	99.4-100.6%	Powder	Ajax Finechem
Citric acid	$C_6H_8O_7$	192.12	99.0%	Powder	Sigma

In the process of preparing $La_{0.3}Sr_{0.7}CoO_3$, $La(NO_3)_3 \cdot 6H_2O$, $Sr(NO_3)_2$ and $Co(NO_3)_2 \cdot 6H_2O$ were mixed in the appropriate amount of deionized water in a big beaker with stirring on a magnetic stirrer. Then EDTA powder was added in the mixture while stirring after dissolved in deionized water followed by adding dissolved citric acid. The mole number of EDTA required is as same as the sum of mole numbers of all metal ions and the moles of citric acid is the twice

of that of EDTA. Then, added NH_4OH to adjust the pH value of the solution up to 7. Keep the solution on the magnetic stirrer with high speed and 80°C for about 6 hours until the rotor cannot rotate. Take out the rotor and move the beaker in the oven to burn at 260°C for 8 hours. At last, ground twice before and after calcined in air at 900°C for 4 hours respectively to obtain the final $La_{0.3}Sr_{0.7}CoO_3$ perovskite powder.

The other five samples had the same processes as preparing $La_{0.3}Sr_{0.7}CoO_3$ perovskite powder. The specific amounts of every chemical for each sample are listed in table 2.

Table 2 The amount of chemicals for $La_xSr_{1-x}CoO_3$

0.02mol	$La_{0.7}Sr_{0.3}CoO_3$			$La_{0.5}Sr_{0.5}CoO_3$			$La_{0.3}Sr_{0.7}CoO_3$		
	MW	mol	W/g	MW	mol	W/g	MW	mol	W/g
$La(NO_3)_3.6H_2O$	433.01	0.014	6.06	433.01	0.01	4.33	433.01	0.006	2.60
$Sr(NO_3)_2$	211.63	0.006	1.27	211.63	0.01	2.12	211.63	0.014	2.96
$Co(NO_3)_3.3H_2O$	291.03	0.020	5.82	291.03	0.02	5.82	291.03	0.020	5.82
EDTA	292.25	0.040	11.69	292.25	0.04	11.69	292.25	0.040	11.69
Citric Acid	192.12	0.080	15.37	192.12	0.08	15.37	192.12	0.080	15.37

Table 3 The amount of chemicals for $La_{0.5}Sr_{0.5-x}Ce_xCoO_3$

0.02mol	$La_{0.5}Sr_{0.45}Ce_{0.05}CoO_3$			$La_{0.5}Sr_{0.4}Ce_{0.1}CoO_3$			$La_{0.5}Sr_{0.3}Ce_{0.2}CoO_3$		
	MW	mol	W/g	MW	mol	W/g	MW	mol	W/g
$La(NO_3)_3 \cdot xH_2O$	324.92	0.010	6.06	324.92	0.010	4.33	324.92	0.010	2.60
$Sr(NO_3)_2$	211.63	0.009	1.27	211.63	0.008	2.12	211.63	0.006	2.96
$Ce(NO_3)_3 \cdot 6H_2O$	434.23	0.001	0.43	434.23	0.002	0.87	434.23	0.004	1.74
$Co(NO_3)_3.3H_2O$	291.03	0.020	5.82	291.03	0.020	5.82	291.03	0.020	5.82
EDTA	292.24	0.040	11.69	292.24	0.040	11.69	292.24	0.040	11.69
Citric Acid	192.12	0.080	15.37	192.12	0.080	15.37	192.12	0.080	15.37

3.2 Materials characterization and electrochemical measurement

3.2.1 X-ray Powder Diffraction (XRD)

To identify the crystal structure of the perovskite samples, X-ray Powder Diffraction tests were conducted. The apparatus used for tests was a Bruker D8 Advance MKII XRD to get the X-ray diffraction patterns which have 2θ from 10° to 90°. The scan rate was 0.1°/step with a nickel-filtered Cu kα radiation.

Also, the crystallite size can be calculated from the data abstracted from XRD pattern using the Scherrer formula:

$$D_p = (0.94 \times \lambda)/(\beta \times Cos\theta) \quad (33)$$

Where D_p is the calculated average crystallite size, λ is the X-ray wavelength with the constant of Cu kα laser 0.15418, β is the line broadening in radians and θ is the Bragg angle.

3.2.2 X-ray photoelectron spectroscopy (XPS)

To analysize the elements within a film of perovskite samples and metals state for the metal oxides (mainly cobalt), X-ray photoelectron spectroscopy test was used in the experiment. The X-ray analysis facility was equipped with state of the art Kratos Axis Ultra photoelectron spectrometer using monochromatic Al kα (1486.6 eV) x-rays and 165 mm hemispherical electron energy analyser.

The first step of processing the XPS spectra was tuning the binding energy of C 1s line to 284.6 eV as a reference to unify the data.

3.2.3 Brunauer-Emmett-Teller (BET) surface area

To get the surface area, Brunauer-Emmett-Teller theory was used to analyse. The equipment used was a Micrometritics TriStar II 3020 and the testing environment was nitrogen adsorption as 77 K which is the nitrogen boiling point.

3.2.4 Rotating ring-disk electrode (RRDE) electrochemical test

This experiment used a rotating ring-disk electrode (RRDE) to achieve electrochemical measurement for perovskite samples. The glassy carbon (GC) disk electrode for RRDE test was polished using a PK-3 polishing kit and cleaned in ethanol alcohol with sonication every time before and after use.

The first step was preparing samples for thin film electrode making. 5.0 mg perovskite powder and 5.0 mg carbon black (Alfa Aesar) were mixed with 500 ml ethanol alcohol and 50 μL Nafion solution (5 wt%) before sonicating the mixture for at least 20 minutes to make sure they are evenly distributed in suspension. After sonicating, 5 μL suspension was moved on a GC electrode with 0.4 cm diameter using a pipette and dried until ethanol evaporated.

Experimental facility for RRDE test was Biologic VMP2/Z multichannel potentiostat which was a three-electrode cell configuration. The reference electrode was Ag | AgCl (KCl), and the counter electrode was Pt wire immersed in oxygen saturated KOH solution (0.1 M) respectively. The oxygen saturated electrolyte was achieved by slowly bubbling O_2 (99.99% purity) during the whole testing process. The rotate speed was set at 1600 rpm.

Before collecting data, Linear Voltammetry Experiment was used to remove the bubble on the surface of the film. To get the ORR polarization curve, Linear Voltammetry Experiment was used again setting sweep potential from -0.6 volts to 0.1 volts at a sweep rate of 0.005 V/sec, while to get the OER performance data, Cyclic Voltammetry Experiment was used setting sweep potential between 0 volts to 0.9 volts for three circles at a sweep rate of 0.01 V/sec. The compensated calculating formula of potentials in this report was listed as follows:

$$E(v) = E_{Ag|AgCl} + E_{RE} - iR_u \tag{34}$$

Where $E_{Ag|AgCl}$ was the potential and i was the current got from test, E_{RE} was obtained by the calibration of the reference electrode (Ag|AgCl, KCl) in electrolyte PH = 13 which was 0.973 V, and R_u was the ohmic resistance between the reference electrode and the surface of the working electrode in electrolyte PH = 13 which was 55 Ω. The current density j (mA/cm^2) was calculated using the formula (2) as follows:

$$j\left(\frac{mA}{cm^2}\right) = i/A_{gc} \tag{35}$$

Where A_{gc} was the effective area of the GC electrode.

4. Results and discussions

4.1 Phenomenon during synthesis

An obvious difference between $La_xSr_{1-x}CoO_3$ and $La_{0.5}Sr_{0.5-x}Ce_xCoO_3$ during the synthesis process was found that $La_{0.5}Sr_{0.5-x}Ce_xCoO_3$ samples blew open in the stage of burning in the oven at 260°C and they got a larger volume than the $La_xSr_{1-x}CoO_3$ samples after burning. This phenomenon was speculated that caused by the presentence of cerium.

4.2 XRD for $La_xSr_{1-x}CoO_3$

X-ray diffraction patterns is a practical way to investigate the structure of nanomaterials and their phase purity. The XRD patterns of $La_xSr_{1-x}CoO_3$ are shown in Figure 18. According to the data in the article of Yajun Zhao et al. (2018), compared the peaks in Figure 18 with the standard

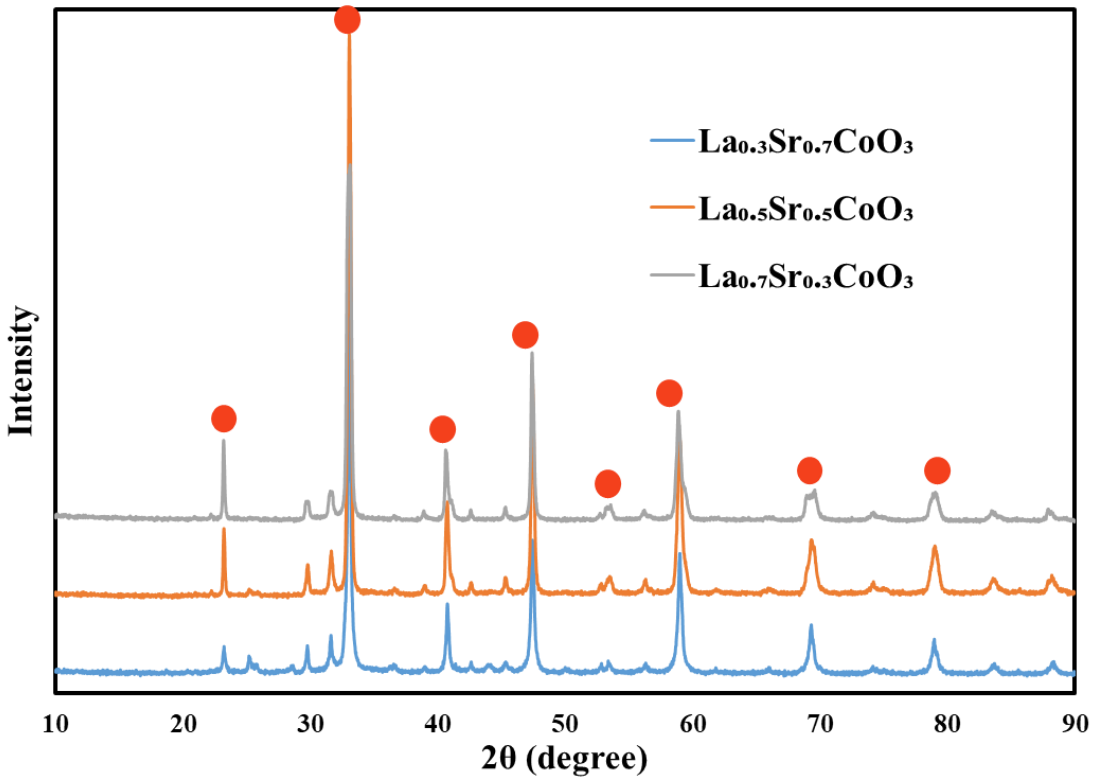

Figure 18. X-ray diffraction (XRD) patterns for LaxSr1-xCoO3.

PDF card, they conform the cubic perovskite structure. Also, there is no other obvious phases and impurities detected in the patterns except the two peaks aside the highest peak. The two

peaks are caucused by instrument error that almost every sample would get these two peaks in their patterns. Thus, the three samples can be regarded as purity perovskite structures.

The average grain size of samples can be calculated through Scherrer equation ("XRD Crystallite Size Calculator (Scherrer Equation)," 2019) using the (110) peak (second peak from the left in Figure 18) data (Zhao et al., 2018). The processes of getting the data as follows:

Open the XRD pattern of the material obtained from the instrument. Zoom on the area that will be calculated its crystallite size and note down the angle and peak full width at half maximum (FWHM). Thus, the calculated results of the crystallite size can be got from the filed on the website. According to the analysis by MDI Jade 6.5, the (110) peak position (2θ) and FWHM (2θ) of $La_{0.3}Sr_{0.7}CoO_3$ are 33.64 and 0.263 respectively, and X-ray wavelength for Cu Kα laser is 0.15148. Thus, the average grain size is 32.97 nm. Using the same method to get data of three samples and the results are listed in the follows.

Table 4 Grain size calculating data of $La_xSr_{1-x}CoO_3$

Samples	$La_{0.3}Sr_{0.7}CoO_3$	$La_{0.5}Sr_{0.5}CoO_3$	$La_{0.7}Sr_{0.3}CoO_3$
Peak Position (2θ)	33.64	33.66	33.71
FWHM (2θ)	0.263	0.276	0.381
X-Ray Wavelength	0.15418	0.15418	0.15418
Grain Size / nm	32.97	31.42	22.76

The results indicate that with the increased content of La, the particle sizes show a decreasing trend.

4.3 XPS for $La_xSr_{1-x}CoO_3$

Further analysis of surface composition and Co valence for $La_xSr_{1-x}CoO_3$ were investigated by XPS, shown in Figure 19. The overall XPS spectrum of $La_{0.5}Sr_{0.5}CoO_3$ is shown in Figure 19(a),

which contains all elements and is similar to the other two samples. The other three figures are Co2p spectra with the value of Co^{2+}/Co^{3+} labelled on.

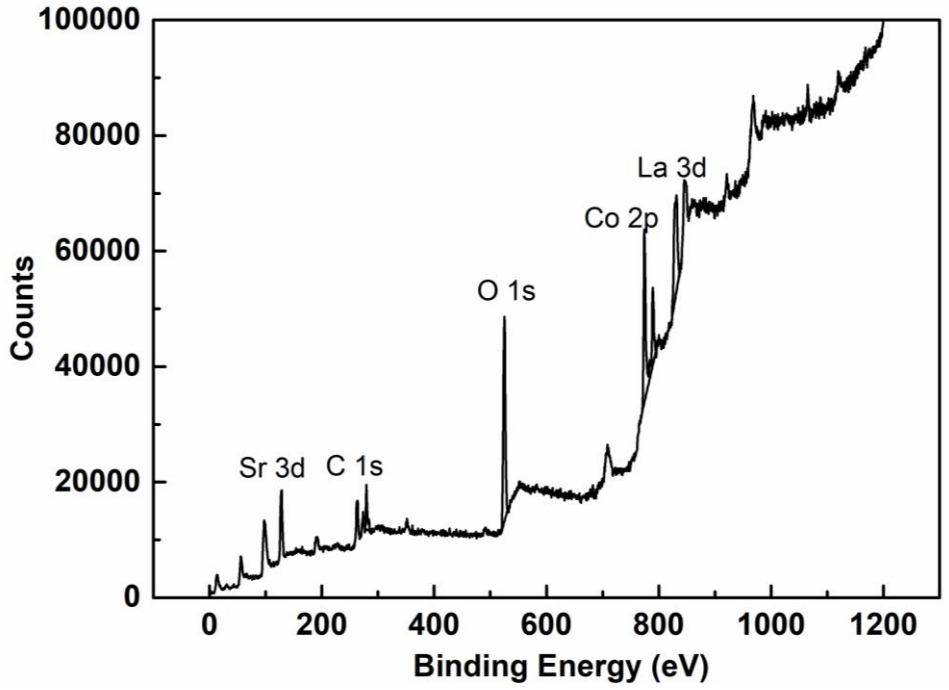

Figure 19(a). The overall XPS spectrum for $La_{0.5}Sr_{0.5}CoO_3$.

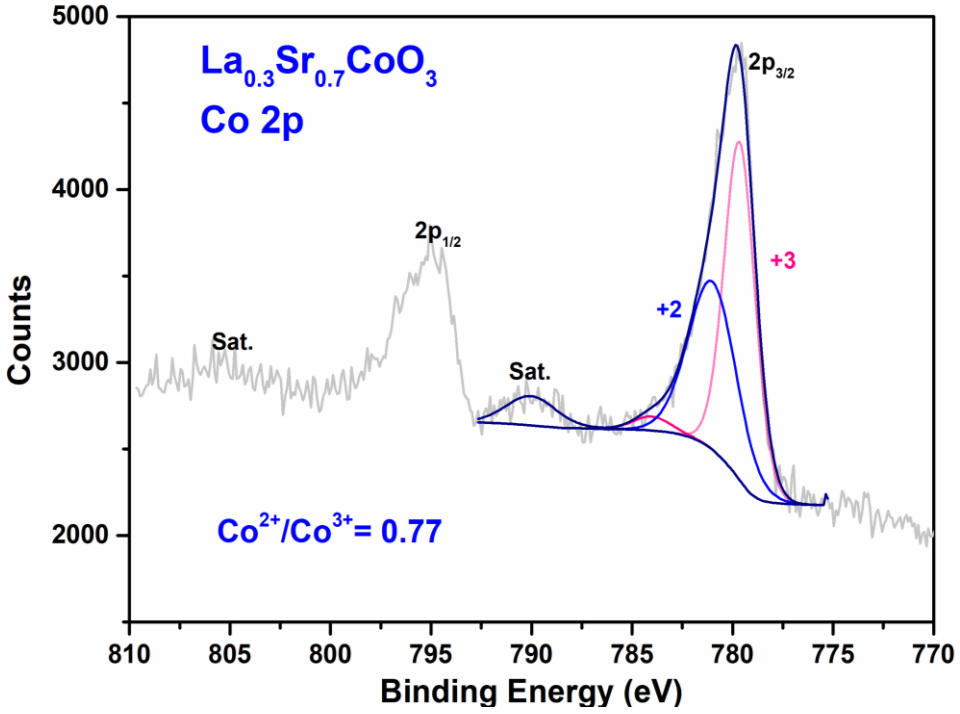

Figure 19(b). Co2p XPS pattern for $La_{0.3}Sr_{0.7}CoO_3$.

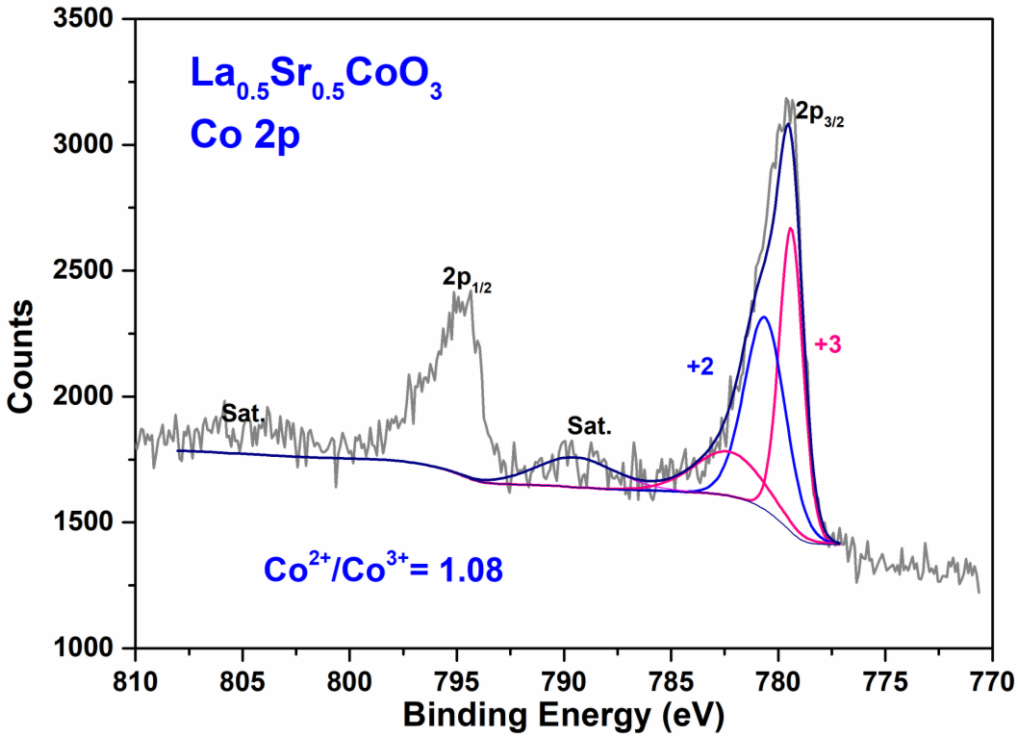

Figure 19(c). Co2p XPS pattern for $La_{0.5}Sr_{0.5}CoO_3$.

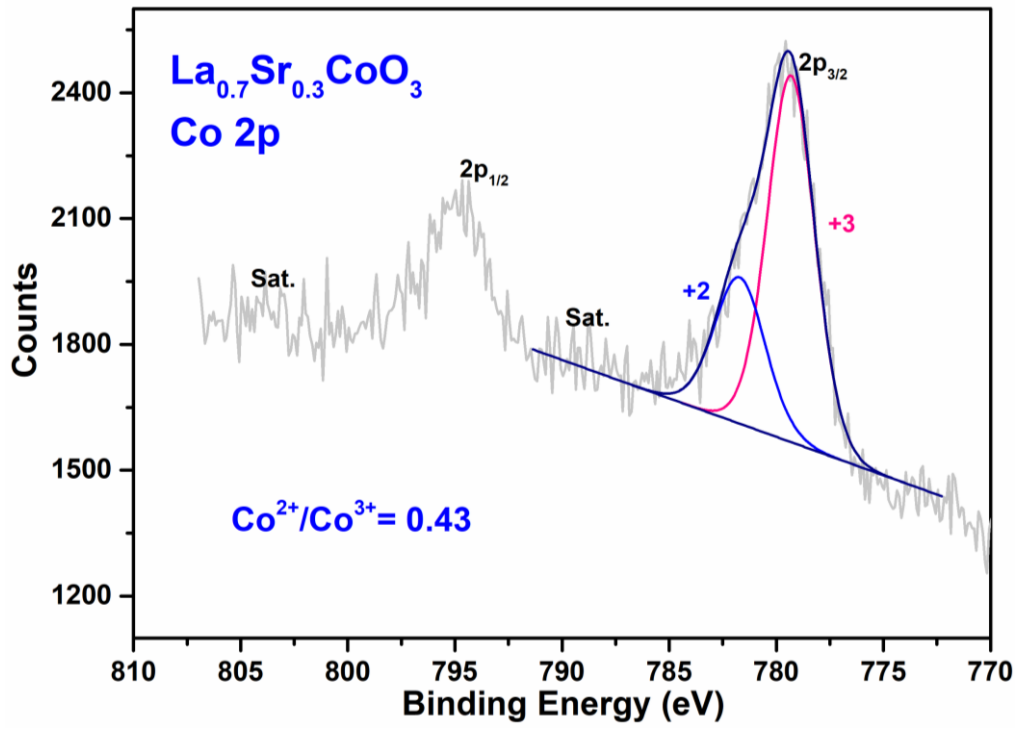

Figure 19(d). Co2p XPS pattern for $La_{0.7}Sr_{0.3}CoO_3$.

According to the three patterns above, Co2p has two peaks, for which the peak around 780 eV is assigned to $Co2p_{3\backslash2}$ and the peak around 795 eV is assigned to $Co2p_{1\backslash2}$. Both of $Co2p_{3\backslash2}$ and

$Co2p_{1\2}$ combine with satellite peaks and they can be split into two peaks for Co^{2+} and Co^{3+}. It can be seen from the area ration of Co^{2+} and Co^{3+}, $La_{0.5}Sr_{0.5}CoO_3$ has the largest content of Co^{2+}. Zhang et al. have conducted the density functional theory calculations, which improved that Co^{2+} defects have lower formation energy than Co^{3+} defects (R. Zhang et al., 2018). That is to say, most of the cobalt vacancies are Co^{2+} defects and Co^{2+} contributes to forming oxygen vacancies. Also, previous studies have improved that oxygen vacancies can contribute to the OER performance (Lu, Yip, Wang, Huang, & Zhou, 2012; T. Y. Ma, Zheng, Dai, Jaroniec, & Qiao, 2014; Trahey et al., 2011),thereby samples with more Co^{2+} content might have better OER performance. In this case, $La_{0.5}Sr_{0.5}CoO_3$ can be assumed as the best catalyst among the three samples.

4.4 BET for $La_xSr_{1-x}CoO_3$

The data BET surface area of three samples get from Micrometritics TriStar II 3020 are listed below.

Table 5 BET surface area of $La_xSr_{1-x}CoO_3$

Samples	$La_{0.3}Sr_{0.7}CoO_3$	$La_{0.5}Sr_{0.5}CoO_3$	$La_{0.7}Sr_{0.3}CoO_3$
Surface area/m^2g^{-1}	6.7798	2.5533	6.9352

Three samples have a surface area in the same order of magnitude. Compared with other samples, the lanthanum, strontium and cobalt-based perovskite synthesized by EDTA-citrate complexing method does not have a large specific surface area. Normally, catalysts with the large surface area have better catalytic performance because of the large contact area, and the surface area is also related to the performance results. Thus, the data of surface area are used to divide the data from electrochemical test to get more exact results about their OER and ORR performance.

4.5 OER/BET for $La_xSr_{1-x}CoO_3$

To prove the assumption above, electrochemical measurement using a rotating ring-disk electrode (RRDE) was conducted to compare their OER performance. The results of their OER performance verses BET surface area are listed in the follows.

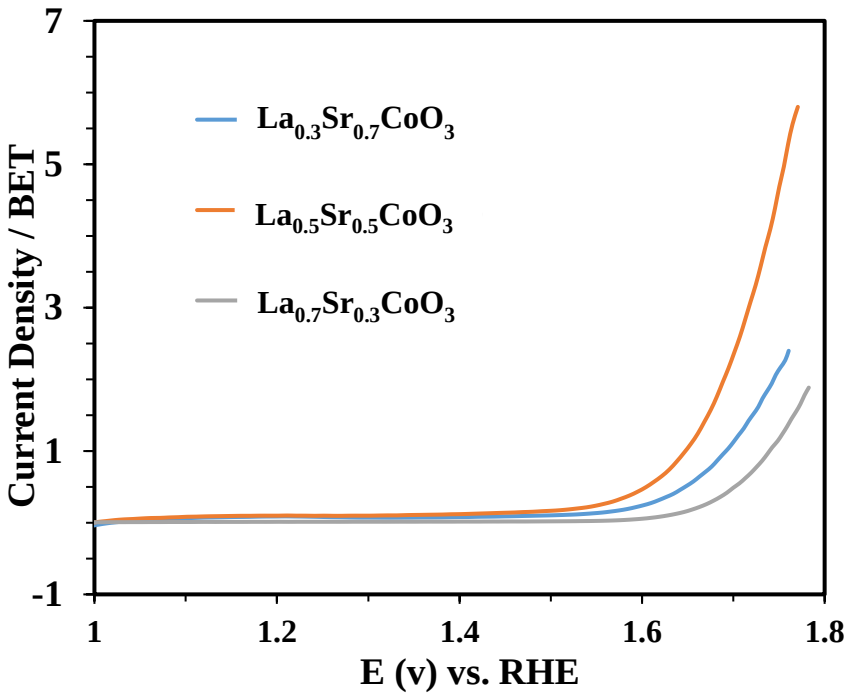

Figure 20. OER / BET currents of $La_{0.5}Sr_xCe_{0.5-x}CoO_3$ (x=0.05, 0.1, 0.2) perovskite oxides.

After dividing the OER data by BET surface area, Figure 20 shows clearly that $La_{0.5}Sr_{0.5}CoO_3$ has the highest value of OER/BET among the three samples which confirms the previous assumption. For the other two samples, $La_{0.3}Sr_{0.7}CoO_3$ performs better than $La_{0.7}Sr_{0.3}CoO_3$.

4.6 ORR/BET for $La_xSr_{1-x}CoO_3$

Similar to OER performance, to compare the ORR performance of three samples, the results of their ORR verses BET surface area are listed in the follows.

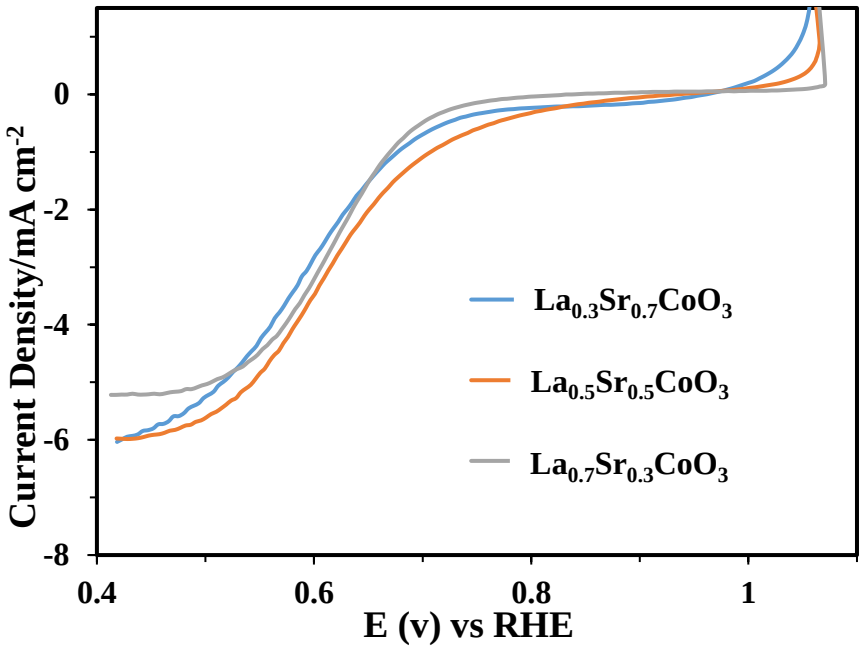

Figure 21. ORR / BET currents of $La_{1-x}Sr_xCoO_3$ (x=0.3, 0.5, 0.7) perovskite oxides.

Figure 21 shows that $La_{0.5}Sr_{0.5}CoO_3$ is still the one with the best ORR performance among the three samples.

According to the test results above, $La_{0.5}Sr_{0.5}CoO_3$ is the one with the best catalytic performance. So, $La_{0.5}Sr_{0.5}CoO_3$ was chosen to verify furtherly about the effect of Ce-doping as the basis, which means for the cerium-doping sample, the amounts of lanthanum on A-site are 0.5 for all the samples, and the only changes of the amount is the ratio of strontium and cerium.

4.7 XRD for $La_{0.5}Sr_{0.5-x}Ce_xCoO_3$

The XRD patterns of $La_{0.5}Sr_{0.5-x}Ce_xCoO_3$ are shown in Figure 22. Compared with the patterns of $La_xSr_{1-x}CoO_3$, all of them have the same seven peaks, which means that the Ce-doped samples are cubic system and they were synthesized to perovskite structure successfully. There are also obvious peaks around 28 degrees for $La_{0.5}Sr_{0.4}Ce_{0.1}CoO_3$ and $La_{0.5}Sr_{0.3}Ce_{0.2}CoO_3$ which is cerium oxides showing in PDF cards. This indicates that cerium is doped in the perovskite successfully.

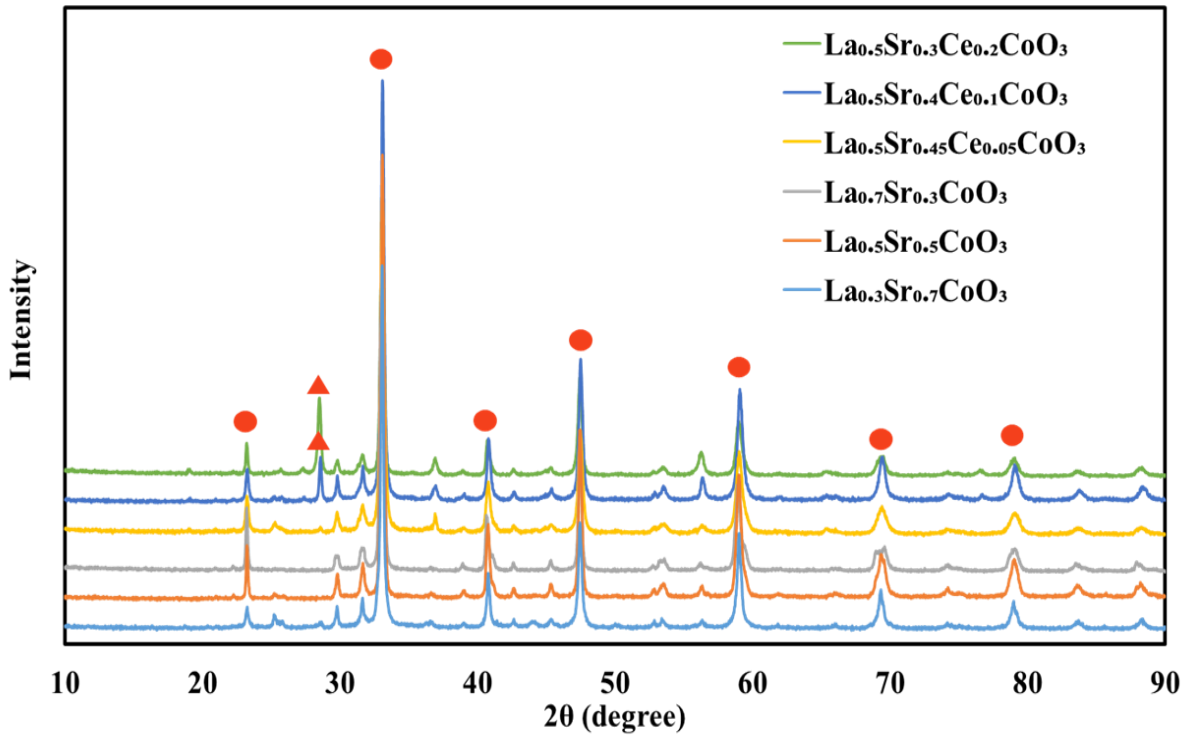

Figure 22. X-ray diffraction (XRD) patterns for $La_xSr_{1-x}CoO_3$ and $La_{0.5}Sr_{0.5-x}Ce_xCoO_3$.

Using the same method to get the average grain size as follows. There is no obvious rule among the three samples, but all of them have a smaller grain size than $La_{0.5}Sr_{0.5}CoO_3$, which means that Ce-doping might decreases the grain size of perovskite.

Table 6 Grain size calculating data of $La_{0.5}Sr_{0.5-x}Ce_xCoO_3$

Samples	$La_{0.5}Sr_{0.45}Ce_{0.05}CoO_3$	$La_{0.5}Sr_{0.4}Ce_{0.1}CoO_3$	$La_{0.5}Sr_{0.3}Ce_{0.2}CoO_3$
Peak Position (2θ)	33.64	33.661	33.659
FWHM (2θ)	0.326	0.277	0.302
X-Ray Wavelength	0.15418	0.15418	0.15418
Grain Size / nm	26.60	31.31	28.72

4.8 XPS for $La_{0.5}Sr_{0.5-x}Ce_xCoO_3$

The overall XPS spectrum of $La_{0.5}Sr_{0.4}Ce_{0.1}CoO_3$ is shown in Figure 23(a), which contains all elements and is similar to the other two Ce-doping samples. The obvious difference with Figure 23(a) is that it has Ce3d peaks around 900 eV which are zoomed out and split in Figure 23(b).

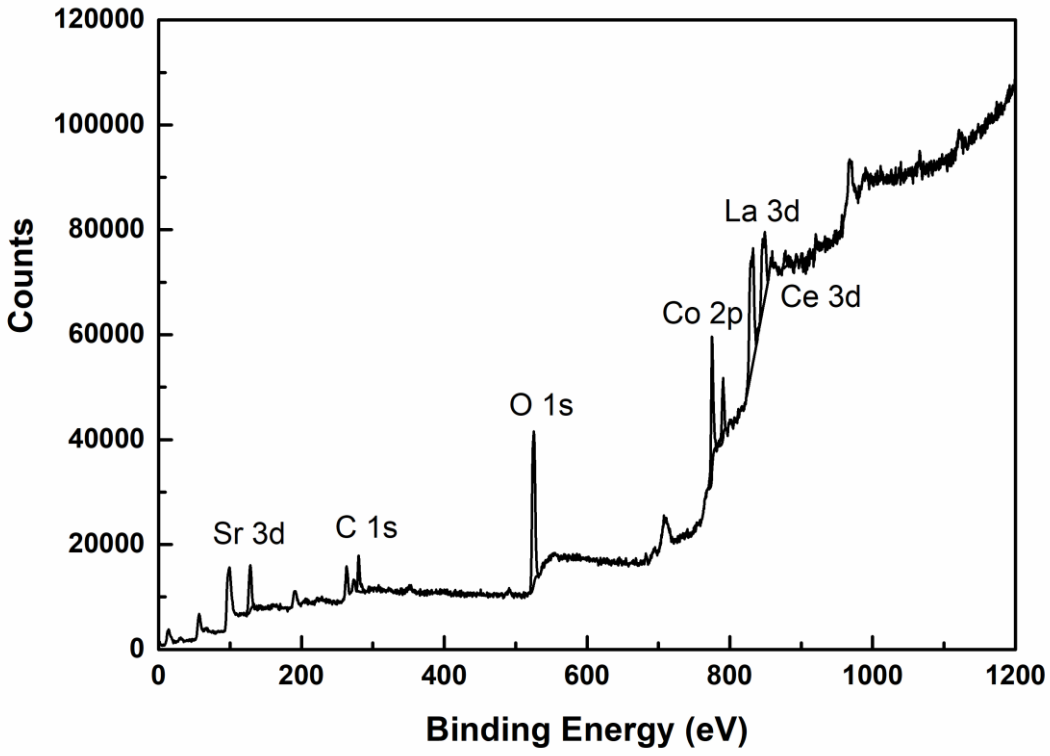

Figure 23(a). The overall XPS spectrum for La0.5Sr0.4Ce0.1CoO3.

Figure 23(b) is the Ce3d spectrum of $La_{0.5}Sr_{0.4}Ce_{0.1}CoO_3$. The peaks from 880 eV to 900 eV denote $Ce3d_{5/2}$ and peaks from 900 eV to 915 eV correspond to $Ce3d_{3/2}$. These peaks show that Ce was doped in the perovskite successfully. The other two Ce-doped samples have similar Ce3d peaks with Figure 23(b).

Figure 23(c, d, e) are the Co2p spectra of three Ce-doped samples with the value of Co^{2+}/Co^{3+} labelled on.

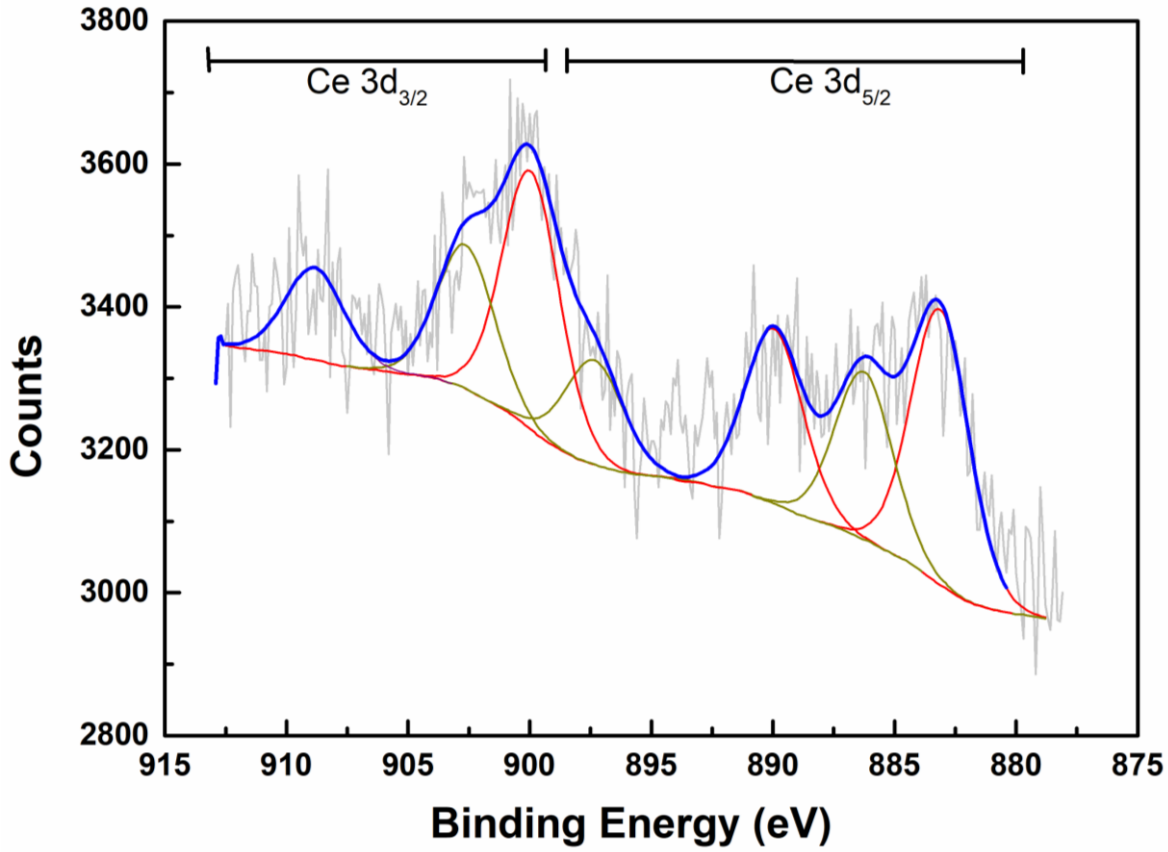

Figure 23(b). Ce3d XPS spectrum for La0.5Sr0.4Ce0.1CoO3.

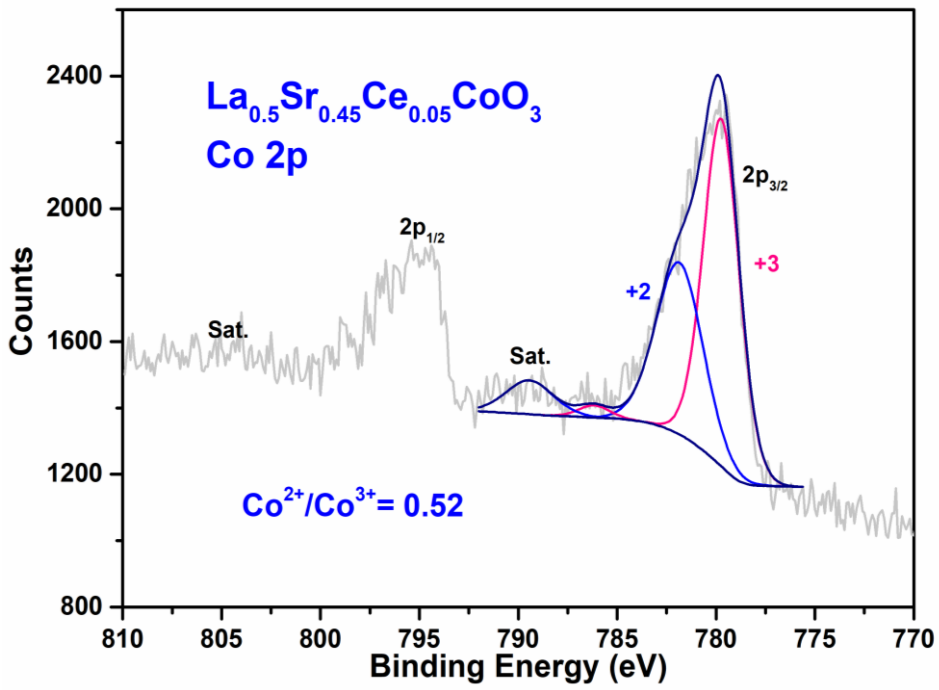

Figure 23(c). Co2p XPS pattern for $La_{0.5}Sr_{0.45}Ce_{0.05}CoO_3$.

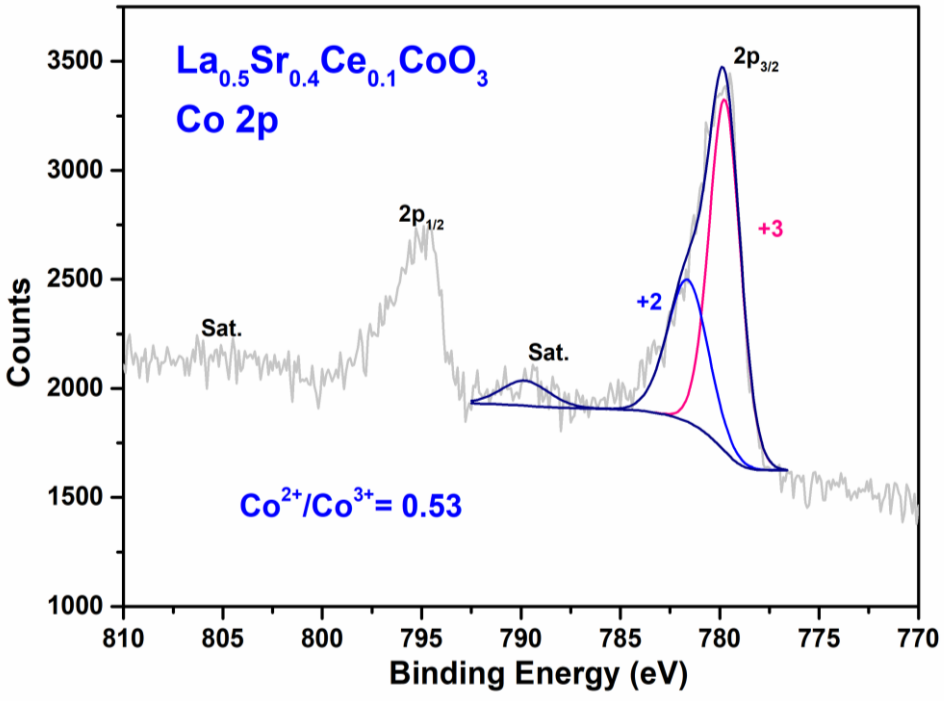

Figure 23(d). Co2p XPS pattern for $La_{0.5}Sr_{0.4}Ce_{0.1}CoO_3$.

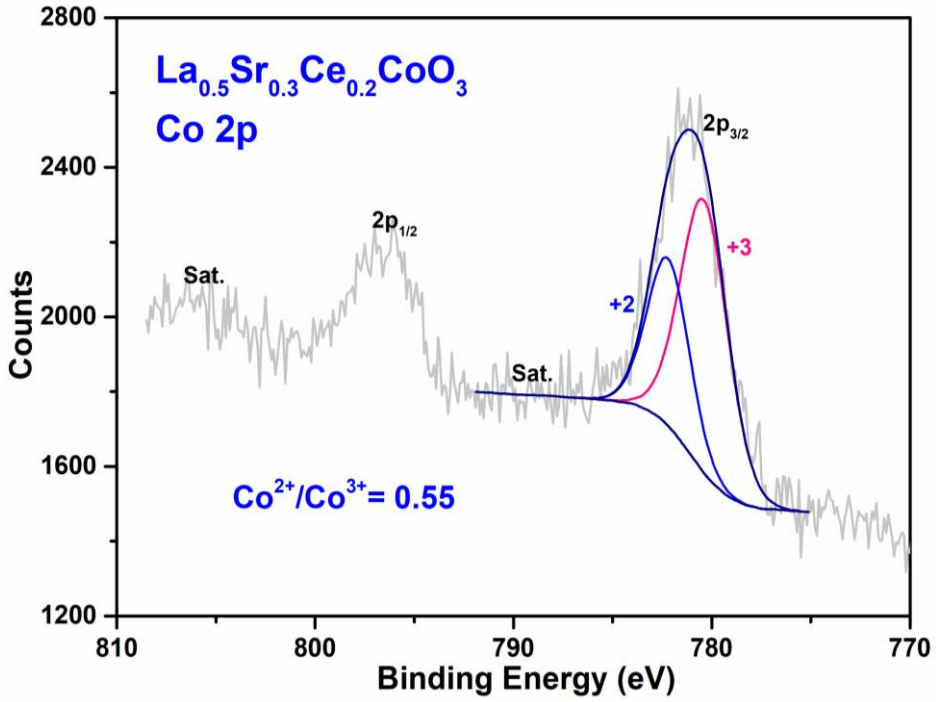

Figure 23(e). Co2p XPS pattern for $La_{0.5}Sr_{0.3}Ce_{0.2}CoO_3$.

Same to the previous analysis about Co^{2+}/Co^{3+} effecting the OER performance, it can be seen from the area ration of Co^{2+} and Co^{3+}, has the largest content of Co^{2+} among the three Ce-doped samples. In this case, $La_{0.5}Sr_{0.3}Ce_{0.2}CoO_3$ can be assumed as the best catalyst among the three now samples.

4.9 BET for $La_{0.5}Sr_{0.5-x}Ce_xCoO_3$

The data BET surface area of three samples get from Micrometritics TriStar II 3020 are listed below.

Table 7 BET surface area of $La_{0.5}Sr_{1-x}Ce_xCoO_3$

Samples	$La_{0.5}Sr_{0.45}Ce_{0.05}CoO_3$	$La_{0.5}Sr_{0.4}Ce_{0.1}CoO_3$	$La_{0.5}Sr_{0.3}Ce_{0.2}CoO_3$
Surface area/m^2g^{-1}	6.9053	4.773	3.3537

The data have the same order of magnitude as the previous samples and the cerium-doped samples still have a small surface area as before. So that the OER and ORR data are needed to be divided by the specific surface area.

4.10 OER/BET for $La_{0.5}Sr_{0.5-x}Ce_xCoO_3$

To prove the assumption above and compare OER performance between the three Ce-doped samples and $La_{0.5}Sr_{0.5}CoO_3$, electrochemical measurement using a rotating ring-disk electrode (RRDE) was conducted. The results of their OER performance verses BET surface area are listed in the follows.

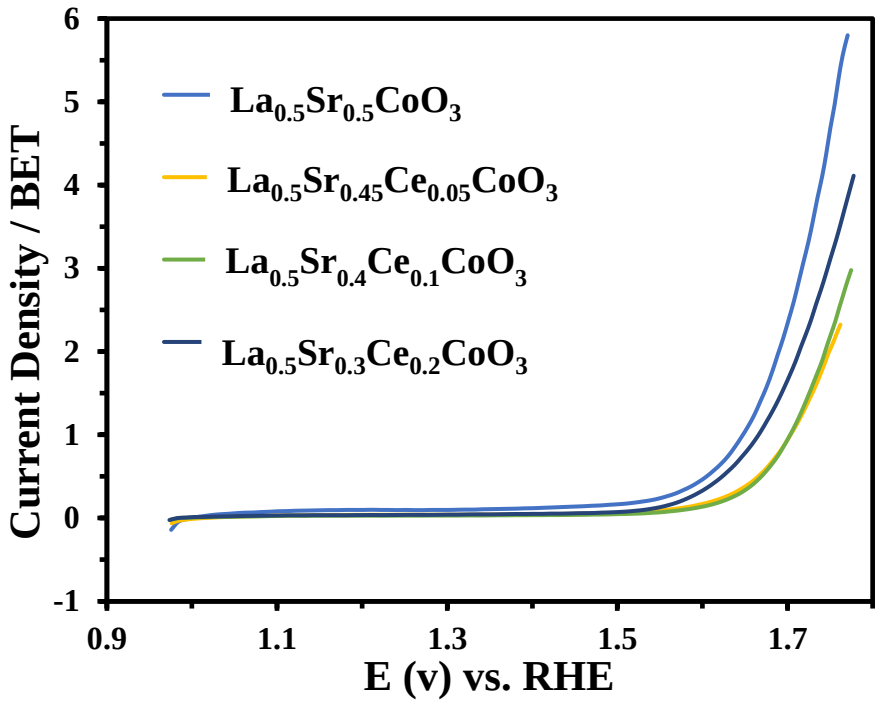

Figure 24. OER / BET currents of $La_{0.5}Sr_xCe_{0.5-x}CoO_3$ (x=0.05, 0.1, 0.2) perovskite oxides compared with $La_{0.5}Sr_{0.5}CoO_3$.

Compared with three Ce-doped samples, $La_{0.5}Sr_{0.5}CoO_3$ is still the one with the best OER performance according to the RRDE test. However, it is also clear that with the increase of the doping amount of cerium, the OER performance is getting better. This illustrates that Ce-doping could improve OER performance. Thus a reasonable conjecture can be raised that a better OER performance than the La0.5Sr0.5CoO3 result might be detected with a larger amount of cerium doping in the sample. Further study can be done to synthesize larger amount of Ce-doping perovskite, for example, $La_{0.5}Sr_{0.1}Ce_{0.4}CoO_3$ and $La_{0.5}Ce_{0.5}CoO_3$ to verify this statement.

4.11 ORR/BET for $La_{0.5}Sr_{0.5-x}Ce_xCoO_3$

To compare the ORR performance of three samples and $La_{0.5}Sr_{0.5}CoO_3$, the results of their ORR verses BET surface area are listed in the follows.

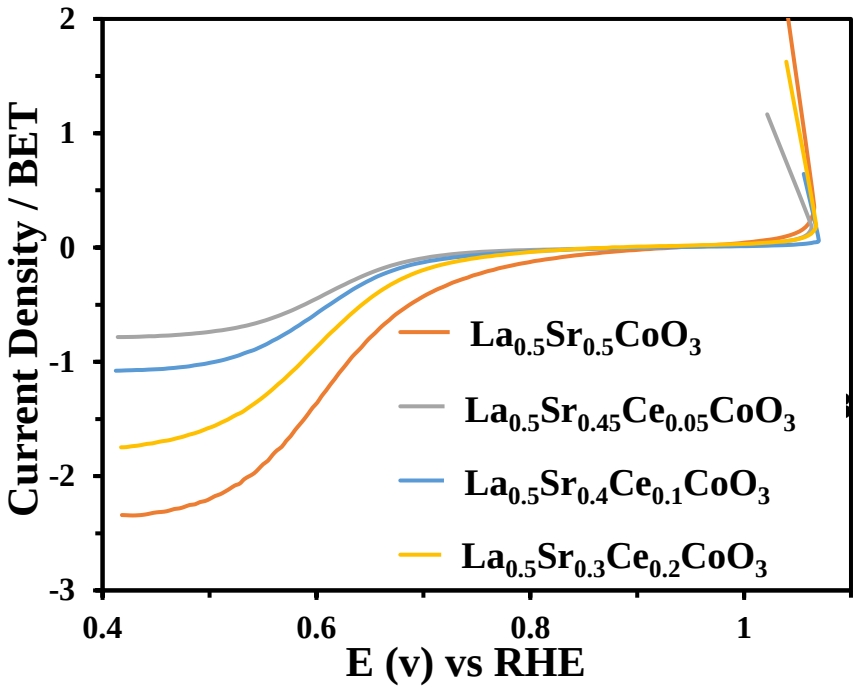

Figure 25. ORR / BET currents of $La_{0.5}Sr_xCe_{0.5-x}CoO_3$ (x=0.05, 0.1, 0.2) perovskite oxides compared with $La_{0.5}Sr_{0.5}CoO_3$.

The lower current density is, the better the ORR performance it has. According to the figure above, similar to the OER results, $La_{0.5}Sr_{0.5}CoO_3$ still has the best ORR performance among all of the samples. Not like the previous three samples that have close data, the cerium-doped samples have a clear difference and the larger amount of cerium samples have better performance. It is further improved that conjecture above is reasonable.

5. Conclusion

Perovskite-type catalysts have good OER and ORR performance and compared with the noble based oxides; these catalysts have lower cost that suitable for commercial usage. After the characterization tests for the six samples, it is proved that the perovskite-type catalysts can be synthesized through EDTA-citric complexing method successfully, but samples synthesized by this method have small specific surface areas. As for the particle size, the doping of cerium can decrease the number. Among the six samples, $La_{0.5}Sr_{0.5}CoO_3$ has the best OER and ORR performance, even compared with the cerium-doped samples. So, $La_{0.5}Sr_{0.5}CoO_3$ was used as the basis to research the effect of doping cerium. The results show that as the increase of the amount of cerium doping, the samples have better properties. In this case, further studies can be done to synthesize larger amount of cerium-doped samples like $La_{0.5}Sr_{0.1}Ce_{0.4}CoO_3$ and even $La_{0.5}Ce_{0.5}CoO_3$ to investigate their performance.

References

Arungovind, M., Purushotham, K. G., Arunkumar, J., & Sendilvelan, S. (2017). Analysis of microbial fuel cell for energy harvesting with waste water and molasses. *International Journal of pharma and Bio Science, 8*(1). doi:10.22376/ijpbs.2017.8.1.b63-69

Audichon, T., Napporn, T. W., Canaff, C., Morais, C., Comminges, C., & Kokoh, K. B. (2016). IrO2 Coated on RuO2 as Efficient and Stable Electroactive Nanocatalysts for Electrochemical Water Splitting. *The Journal of Physical Chemistry C, 120*(5), 2562-2573. doi:10.1021/acs.jpcc.5b11868

Awad, N. K., Ashour, E. A., & Allam, N. K. (2014). Recent advances in the use of metal oxide-based photocathodes for solar fuel production. *Journal of Renewable and Sustainable Energy, 6*(2). doi:10.1063/1.4871899

BET theory. (2019, May 21). *Wikipedia*. Retrieved from https://en.wikipedia.org/wiki/BET_theory

Browne, M. P., & Mills, A. (2018). Determining the importance of the electrode support and fabrication method during the initial screening process of an active catalyst for the oxygen evolution reaction. *Journal of Materials Chemistry A, 6*(29), 14162-14169. doi:10.1039/c8ta02908c

Cesar, I., Kay, A., Gonzalez Martinez, J. A., & Gratzel, M. (2006). Translucent thin film Fe2O3 photoanodes for efficient water splitting by sunlight: nanostructure-directing effect of Si-doping. *J Am Chem Soc, 128*(14), 4582-4583. doi:10.1021/ja060292p

Characterization (materials science). (2019, May 25). *Wikipedia*. Retrieved from https://en.wikipedia.org/wiki/Characterization_(materials_science)

Cheng, F., & Chen, J. (2012). Metal-air batteries: from oxygen reduction electrochemistry to cathode catalysts. *Chem Soc Rev, 41*(6), 2172-2192. doi:10.1039/c1cs15228a

Choi, H.-A., Jang, H., Hwang, H., Choi, M., Lim, D., Shim, S. E., & Baeck, S.-H. (2014). Synthesis and characterization of different MnO2 morphologies for lithium-air batteries. *Electronic Materials Letters, 10*(5), 957-962. doi:10.1007/s13391-014-4066-x

Conway, B. E., & Tilak, B. V. (2002). Interfacial Processes Involving Electrocatalytic Evolution and Oxidation of H2 and the Role of Chemisorbed H. *Electrochimica Acta*, 3571-3594.

Dutrow, B. L., & Clark, C. M. (Producer). (2019, May 24). X-ray Powder Diffraction (XRD). *Geochemical Instrumentation and Analysis*. Retrieved from https://serc.carleton.edu/research_education/geochemsheets/techniques/XRD.html

Exchange Current Density. (2019, May 21). *Corrosionpedia*. Retrieved from https://www.corrosionpedia.com/definition/477/exchange-current-density

Forgie, R., Bugosh, G., Neyerlin, K. C., Liu, Z., & Strasser, P. (2010). Bimetallic Ru electrocatalysts for the OER and electrolytic water splitting in acidic media. *Electrochemical Solid-State Letters, 13*(4), B36-B39. doi:10.1149/1.3290735

Hunter, B. M., Gray, H. B., & Muller, A. M. (2016). Earth-Abundant Heterogeneous Water Oxidation Catalysts. *Chem Rev, 116*(22), 14120-14136. doi:10.1021/acs.chemrev.6b00398

International Energy Outlook 2018. (2019, May 2). *U.S. Energy Information Administration*. Retrieved from https://www.eia.gov/outlooks/ieo/

Jia, Z., Yin, G., & Zhang, J. (2014). 6 - Rotating Ring-Disk Electrode Method. In *Rotating Electrode Methods and Oxygen Reduction Electrocatalysts* (pp. 199-229): Elsevier.

Lee, J., Yun, J., Kwon, S. R., Chang, W. J., Nam, K. T., & Chung, T. D. (2017). Reverse Electrodialysis-Assisted Solar Water Splitting. *Sci Rep, 7*(1), 12281. doi:10.1038/s41598-017-12476-3

Lee, Y., Suntivich, J., May, K. J., Perry, E. E., & Shao-Horn, Y. (2012). Synthesis and Activities of Rutile IrO2 and RuO2 Nanoparticles for Oxygen Evolution in Acid and Alkaline Solutions. *Journal of Physical Chemistry Letters, 3*(3), 399-404. doi:10.1021/jz2016507

Li, G., Li, S., Ge, J., Liu, C., & Xing, W. (2017). Discontinuously covered IrO2–RuO2@Ru electrocatalysts for the oxygen evolution reaction: how high activity and long-term durability can be simultaneously realized in the synergistic and hybrid nano-structure. *Journal of Materials Chemistry A, 5*(33), 17221-17229. doi:10.1039/c7ta05126c

Lu, Z., Yip, C.-T., Wang, L., Huang, H., & Zhou, L. (2012). Hydrogenated TiO2Nanotube Arrays as High-Rate Anodes for Lithium-Ion Microbatteries. *ChemPlusChem, 77*(11), 991-1000. doi:10.1002/cplu.201200104

Lyu, F., Wang, Q., Choi, S. M., & Yin, Y. (2019). Noble-Metal-Free Electrocatalysts for Oxygen Evolution. *Small, 15*(1), e1804201. doi:10.1002/smll.201804201

Ma, T. Y., Zheng, Y., Dai, S., Jaroniec, M., & Qiao, S. Z. (2014). Mesoporous MnCo2O4with abundant oxygen vacancy defects as high-performance oxygen reduction catalysts. *J. Mater. Chem. A, 2*(23), 8676-8682. doi:10.1039/c4ta01672f

Ma, Z., Zhang, Y., Liu, S., Xu, W., Wu, L., Hsieh, Y.-C., . . . Wang, J. X. (2018). Reaction mechanism for oxygen evolution on RuO2, IrO2, and RuO2@IrO2 core-shell nanocatalysts. *Journal of Electroanalytical Chemistry, 819*, 296-305. doi:10.1016/j.jelechem.2017.10.062

Man, I. C., Su, H.-Y., Calle-Vallejo, F., Hansen, H. A., Martínez, J. I., Inoglu, N. G., . . . Rossmeisl, J. (2011). Universality in Oxygen Evolution Electrocatalysis on Oxide Surfaces. *ChemCatChem, 3*(7), 1159-1165. doi:10.1002/cctc.201000397

Oh, H. S., Nong, H. N., Reier, T., Bergmann, A., Gliech, M., Ferreira de Araujo, J., . . . Strasser, P. (2016). Electrochemical Catalyst-Support Effects and Their Stabilizing Role for IrOx Nanoparticle Catalysts during the Oxygen Evolution Reaction. *J Am Chem Soc, 138*(38), 12552-12563. doi:10.1021/jacs.6b07199

Peng, X., Pi, C., Zhang, X., Li, S., Huo, K., & Chu, P. K. (2019). Recent progress of transition metal nitrides for efficient electrocatalytic water splitting. *Sustainable Energy & Fuels, 3*(2), 366-381. doi:10.1039/c8se00525g

Raja, P. M. V., & Barron, A. R. (Producer). (2019, May 22). BET Surface Area Analysis of Nanoparticles. *Chemistry LibreTexts*. Retrieved from https://chem.libretexts.org/Bookshelves/Analytical_Chemistry/Book%3A_Physical_Methods_in_Chemistry_and_Nano_Science_(Barron)/02%3A_Physical_and_Thermal_Analysis/02.3%3A_BET_Surface_Area_Analysis_of_Nanoparticles

Rotating Ring Disk Electrode (RRDE). (2019, May 23). *BioLogic*. Retrieved from https://www.bio-logic.net/accessories/rotating-ring-disk-electrode/rotating-ring-disk-electrode-rrde/

Sharma, S., Verma, D., Khan, L., Kumar, S., & Khan, S. (2008). *Handbook of Materials Characterization*: Springer International Publishing.

Shin, B. (2016). Electrocatalytic Activity of Co-based Perovskite Oxides for Oxygen Reduction and Evolution Reactions. *International Journal of Electrochemical Science*, 5900-5908. doi:10.20964/2016.07.68

Smart, R., & McIntyre, S. (2019). X-ray Photoelectron Spectroscopy. *City University of Hong Kong City University of Hong Kong*. https://mmrc.caltech.edu/SS_XPS/XPS_PPT/XPS_Slides.pdf

Smith, R. D. L., Prévot, M. S., Fagan, R. D., & Zhang, Z. (2013). Photochemical Route for Accessing Amorphous Metal Oxide Materials for Water Oxidation Catalysis. *Science, 340*(6128), 60-63.

Suen, N. T., Hung, S. F., Quan, Q., Zhang, N., Xu, Y. J., & Chen, H. M. (2017). Electrocatalysis for the oxygen evolution reaction: recent development and future perspectives. *Chem Soc Rev, 46*(2), 337-365. doi:10.1039/c6cs00328a

Tafel equation. (2019, May 23). *Wikipedia*. Retrieved from https://en.wikipedia.org/wiki/Tafel_equation

Tahir, M., Pan, L., Idrees, F., Zhang, X., Wang, L., Zou, J.-J., & Wang, Z. L. (2017). Electrocatalytic oxygen evolution reaction for energy conversion and storage: A comprehensive review. *Nano Energy, 37*, 136-157. doi:10.1016/j.nanoen.2017.05.022

Trahey, L., Johnson, C. S., Vaughey, J. T., Kang, S. H., Hardwick, L. J., Freunberger, S. A., . . . Thackeray, M. M. (2011). Activated Lithium-Metal-Oxides as Catalytic Electrodes for Li–O2 Cells. *Electrochemical and Solid-State Letters, 14*(5). doi:10.1149/1.3555366

Wang, H. (Producer). (2012, November 30). Hydrogen Evolution Reaction. *Stanford University*. Retrieved from http://large.stanford.edu/courses/2012/ph240/wang-ha1/

Wiechen, M., Zaharieva, I., Dau, H., & Kurz, P. (2012). Layered manganese oxides for water-oxidation: alkaline earth cations influence catalytic activity in a photosystem II-like fashion. *Chemical Science, 3*(7). doi:10.1039/c2sc20226c

Working Electrode - GC Glassy Carbon Disk Electrode (2019, May 20). *Select Scientific*. Retrieved from https://selectscientific.com.au/home/index.php/working-electrode-gc-3mm.html

X-ray diffraction. (2019, May 15). *Rigaku* Retrieved from https://www.rigaku.com/en/techniques/xrd

XRD Crystallite Size Calculator (Scherrer Equation). (2019, May 2). *InstaNANO*. Retrieved from https://www.instanano.com/2017/01/xrd-crystallite-size-calculator-scherrer-equation.html

Yamada, Y., Yano, K., Hong, D., & Fukuzumi, S. (2012). LaCoO3 acting as an efficient and robust catalyst for photocatalytic water oxidation with persulfate. *Physical Chemistry Chemical Physics, 14*(16), 5753-5760. doi:10.1039/c2cp00022a

Yan, Y., Xia, B. Y., Zhao, B., & Wang, X. (2016). A review on noble-metal-free bifunctional heterogeneous catalysts for overall electrochemical water splitting. *Journal of Materials Chemistry A, 4*(45), 17587-17603. doi:10.1039/c6ta08075h

Zhang, H. M., Shimizu, Y., Teraoka, Y., Miura, N., & Yamazoe, N. (1989). Oxygen sorption and catalytic properties of La1−xSrxCo1−yFeyO3 Perovskite-type oxides. *Journal of Catalysis, 121*(2), 432-440.

Zhang, R., Zhang, Y.-C., Pan, L., Shen, G.-Q., Mahmood, N., Ma, Y.-H., . . . Zou, J.-J. (2018). Engineering Cobalt Defects in Cobalt Oxide for Highly Efficient Electrocatalytic Oxygen Evolution. *ACS Catalysis, 8*(5), 3803-3811. doi:10.1021/acscatal.8b01046

Zhao, Y., Liu, T., Shi, Q., Yang, Q., Li, C., Zhang, D., & Zhang, C. (2018). Perovskite oxides La 0.4 Sr 0.6 Co x Mn 1-x O 3 (x = 0, 0.2, 0.4) as an effective electrocatalyst for lithium—air batteries. *Green Energy & Environment, 3*(1), 78-85. doi:10.1016/j.gee.2017.12.001

Zou, J. (2018). CHEE 4301 Nanomaterials and their characterisation *UQ blackboard CHEE4301 learning resources*. https://learn.uq.edu.au/bbcswebdav/pid-2731632-dt-content-rid-13492704_1/courses/CHEE4301S_6760_60773/CHEE4301_Lect06.pdf